

1 Crustal structure of southeast Australia from teleseismic 2 receiver functions

3 Mohammed Bello^{1, 2}, David G. Cornwell¹, Nicholas Rawlinson³, Anya M. Reading⁴, Othaniel
4 K. Likkason²

5 ¹Department Geology & Geophysics, University of Aberdeen, Aberdeen, UK

6 ²Department of Physics, Abubakar Tafawa Balewa University, Bauchi, Nigeria

7 ³Department of Earth Sciences, University of Cambridge, UK

8 ⁴School of Natural Sciences (Physics), University of Tasmania, Australia

9 *Correspondence to:* Mohammed Bello (mbazare13@yahoo.com)

10 **Abstract.** In an effort to improve our understanding of the seismic character of the crust beneath southeast
11 Australia, and how it relates to the tectonic evolution of the region, we analyse teleseismic earthquakes recorded
12 by 24 temporary and 8 permanent broadband stations using the receiver function method. Due to the proximity
13 of the temporary stations to Bass Strait, only 13 of these stations yielded usable receiver functions, whereas
14 seven permanent stations produced receiver functions for subsequent analysis. Crustal thickness, bulk seismic
15 velocity properties and internal crustal structure of the southern Tasmanides – an assemblage of Palaeozoic
16 accretionary orogens that occupy eastern Australia – are constrained by H- κ stacking and receiver function
17 inversion, which point to: (1) a ~39.0 km thick crust, an intermediate-high V_p/V_s ratio (~1.70-1.76), relative to
18 ak135, and a broad (>10 km) crust-mantle transition beneath the Lachlan Fold Belt. These results are interpreted
19 to represent magmatic underplating of mafic materials at the base of the crust; (2) a complex crustal structure
20 beneath VanDieland, a putative Precambrian continental fragment embedded in the southernmost Tasmanides,
21 which features strong variability in crustal thickness (23-37 km) and V_p/V_s ratio (1.65-1.93), the latter of which
22 likely represents compositional variability and the presence of melt. The complex origins of Vandieland, which
23 comprises multiple continental ribbons, coupled with recent failed rifting and intraplate volcanism, likely
24 contributes to these observations; and (3) stations located in the East Tasmania Terrane and Eastern Bass Strait
25 (ETT+EB) collectively indicate crust of uniform thickness (31-32 km), which clearly distinguish it from
26 VanDieland to the west. Moho depths are also compared with the continent-wide AusMoho model in southeast
27 Australia, and are shown to be largely consistent, except in regions where AusMoho has few constraints (e.g.
28 Flinders Island). A joint interpretation of the new results with ambient noise, teleseismic tomography and
29 teleseismic shear wave splitting anisotropy, helps provide new insight into the way that the crust has been
30 shaped by recent events, including failed rifting during the break-up of Australia and Antarctica and recent
31 intraplate volcanism.

32 **Keywords:** receiver functions, crustal structure, VanDieland, Bass Strait, SE Australia

33 1 Introduction

34 The Phanerozoic Tasmanides (Collins and Vernon, 1994; Coney, 1995; Coney et al., 1990) comprise the eastern
35 one-third of the Australian continent and through a process of subduction accretion were juxtaposed against the
36 eastern flank of the Precambrian shield region of Australia beginning in the Late Neoproterozoic and Early
37 Palaeozoic (Foster and Gray, 2000; Glen, 2005; Glen et al., 2009; Moresi et al., 2014) (Figure 1). Persistent

sources of debate that impede a more complete understanding of the geology of the Tasmanides include: (1) the geological link between Tasmania – an island state in southeast Australia – and mainland Australia, which are separated by the waters of Bass Strait; and (2) the presence and locations of continental fragments from Rodinian remnants that are entrained within the accretionary orogens. Furthermore, the lateral boundaries between individual tectonic blocks and their crustal structure are often not well defined. To date, few constraints on crustal thickness and seismic velocity structure have been available for regions such as Bass Strait. Constraints on the Moho transition, crustal thickness and velocity structure beneath Bass Strait derived from receiver functions (RFs) can therefore provide fresh insight into the nature and evolution of the Tasmanides.

Previous estimates of crustal thickness and structure beneath southeastern Australia have been obtained from deep seismic reflection transects, wide-angle seismic data, topography and gravity anomalies (e.g. Collins, 1991; Collins et al., 2003; Drummond et al., 2006 and Kennett et al., 2011). Earlier RF studies in southeast Australia (Shibutani et al., 1996; Clitheroe et al., 2000; Tkalčić et al., 2011; Fontaine et al., 2013a,b) suggested the presence of complex lateral velocity variations in the mid-lower crust that probably reflect the interaction of igneous underplating, associated thinning of the lithosphere, recent hotspot volcanism and uplift. Furthermore, the intermediate to high crustal V_p/V_s ratio of 1.70–1.78 in this region (Fontaine et al., 2013a), relative to continental crust where V_p/V_s is ~ 1.68 , may indicate a mafic composition that includes mafic granulite rocks, granite-gneiss and biotite gneiss. Body- and surface-wave tomography (Fishwick and Rawlinson, 2012; Rawlinson et al., 2015) revealed P and S wave velocity anomalies in the uppermost mantle beneath Bass Strait and the Lachlan Fold Belt. Ambient noise surface wave tomography (Bodin et al., 2012b; Young et al., 2012; Pilia et al., 2015b, 2016; Crowder et al., 2019) of the southern Tasmanides revealed significant crustal complexity, but is unable to constrain crustal thickness or the nature of the Moho transition.

The goal of this paper is to provide fresh insight into the crust and Moho structure beneath the southern Tasmanides using P -wave RFs and explain the origin of the lateral heterogeneities that are observed. This will allow us to explore the geological relationship between the different tectonic units that constitute the southern Tasmanides, and develop an improved understanding of the region's tectonic history.

2 Geological setting

The Palaeozoic-Mesozoic Tasmanides of eastern Australia form part of one of the most extensive accretionary orogens in existence and evolved from interaction between the East Gondwana margin and the Proto-Pacific Ocean. The tectonic evolution of the Tasmanides is complex and large-scale reconstructions have proven difficult. This is evident from the variety of models that have been suggested to explain how the region formed (Foster and Gray, 2000; Spaggiari et al., 2003; Teasdale et al., 2003; Spaggiari et al., 2004; Boger and Miller, 2004; Glen, 2005; Cawood, 2005; Glen et al., 2009; Cayley, 2011a,b; Gibson et al., 2011; Moresi et al., 2014; Pilia et al., 2015a,b). Particular challenges arise from multiple subduction events, multiple phases of metamorphism, entrainment of exotic continental blocks, the formation of large oroclinal, recent intraplate volcanism and subsequent events, including the separation of Antarctica and Australia and the formation of the Tasman Sea. These challenges are compounded by the presence of widespread sedimentary sequences that hinder direct access to basement rocks (Fig. 1).

75 The Tasmanides consist of four orogenic belts, namely the Delamerian, Lachlan, Thomson and New England
 76 Orogens. The Delamerian Orogen - located in the south - is the oldest part of the Tasmanides and has a
 77 southward extension across Bass Strait from Victoria into western Tasmania, where it is commonly referred to
 78 as the Tyennan Orogen (Berry et al., 2008). Between about 514 and 490 Ma, the Precambrian and Early
 79 Cambrian rocks that constitute the Delamerian Orogen were subjected to a contractional orogenic event along
 80 the margin of East Gondwana (Foden et al., 2006). Subsequently, the Lachlan Orogen formed in the east, which
 81 contains rocks that vary in age from Ordovician to Carboniferous (Glen, 2005). Gray and Foster (2004) argued
 82 for a tectonic model of the Lachlan Orogen that involved interaction of a volcanic arc, oceanic microplates,
 83 several turbidite thrust systems and three distinct subduction zones. Each subduction zone is linked to the
 84 formation of a distinct tectonic terrain: the Stawell-Bendigo zone, Tabbarebbera zone and Narooma accretionary
 85 complex. The limited rock exposure in the Tasmanides as a whole has made direct observation of the Lachlan
 86 Orogen difficult; this is attributed to a large swath of Mesozoic-Cenozoic sedimentary cover and more recent
 87 Quaternary volcanics, which obscure a large portion of the underlying Palaeozoic terrane. However, the Lachlan
 88 Orogen contain belts of Cambrian rocks in Victoria and New South Wales that are similar in age to the
 89 Delamerian Orogen (Gray and Foster, 2004).

90 The presence of Precambrian outcrops in Tasmania and the relative lack of similar age rocks in adjacent
 91 mainland Australia has led to different models which attempted to explain the existence of Proterozoic
 92 Tasmania. For instance, Li et al. (1997) suggested that western Tasmania may be the remnant of a continental
 93 fragment set adrift by Rodinian break-up, whereas Calvert and Walter (2000) proposed that King Island, along
 94 with western Tasmania, rifted away from the Australian craton around ~600 Ma (Fig. 1). Other researchers have
 95 developed scenarios in which the island of Tasmania was present as a separate microcontinental block that was
 96 positioned outboard of the eastern margin of Gondwana before re-attaching at the commencement of the
 97 Palaeozoic (Berry et al., 2008).

98 A popular model that attempts to reconcile the geology observed in Tasmania and adjacent mainland Australia
 99 is that of Cayley (2011a). This model proposes that central Victoria and western Tasmania formed a
 100 microcontinental block called “VanDieland” that fused with East Gondwana at the end of the Cambrian,
 101 possibly terminating the Delamerian Orogeny. VanDieland became entangled in the subduction-accretion
 102 system which built the Palaeozoic orogens that now comprise eastern Australia (Fig. 1). Delineating
 103 Precambrian continental fragments within southeast Australia has proven difficult, partly due to more recent
 104 sedimentary cover that obscures large tracts of the Tasmanides. However, if present, they likely have distinctive
 105 structural and seismic velocity characteristics (Glen, 2013).

106 **3 Previous geophysical studies**

107 A variety of geophysical methods have so far been deployed to study the crustal structure of the Tasmanides.
 108 Shibutani et al. (1996) applied a non-linear inversion method to RF waveforms to constrain the shear wave
 109 velocity beneath broadband seismic stations in eastern Australia. They found that the Moho is relatively shallow
 110 (30-36 km depth) and sharp within the cratonic region, and deeper (38-44 km) and transitional along the axis of
 111 the Tasmanides. They suggested that crustal thickening of the fold belt by underplating or intrusion of mantle
 112 materials may have contributed to this observation. Clitheroe et al. (2000) built on this earlier work by inverting

113 RFs to map broad-scale crustal thickness and Moho character across the Australian continent. They found that in
 114 general, there was good agreement between xenolith-derived estimates of Moho depth and those determined by
 115 RF inversion, except beneath the Lachlan Fold Belt, where a broad Moho transition may be present. Overall,
 116 however, the RF results were consistent with those determined by Drummond and Collins (1986) and Collins
 117 (1991), who used seismic reflection and refraction transects to determine that the Lachlan Fold Belt includes the
 118 thickest crust (~ 50 km) in eastern Australia. A more recent study by Fontaine et al. (2013a) employed H - κ
 119 stacking and non-linear RF inversion to investigate crustal thickness, shear wave velocity structure, as well as
 120 dipping and anisotropy of the crustal layers. Their results also indicated a thick crust (~ 48 km) and an
 121 intermediate (2-9 km) crust-mantle transition beneath the Lachlan Fold Belt, which could be attributed to
 122 underplating beneath the crust and/or high concentrations of mafic rocks in the mid-lower crust. Their results
 123 also showed a dipping Moho together with crustal anisotropy in the vicinity of three seismic stations (YNG,
 124 CNB and CAN).

125 Over the last decade, ambient noise tomography has become a popular tool for studying the structure of the
 126 Australian crust. Saygin and Kennett (2010) produced the first group velocity maps of the Australian continent
 127 from Rayleigh wave group velocity dispersion in the period range 5.0–12.5 seconds. Limited spatial resolution
 128 ($\sim 2^\circ \times 2^\circ$) in our study region means that this model is only able to represent the structure beneath Bass Strait as
 129 a broad, low velocity anomaly. However, the group velocities exhibit a good correlation with known basins and
 130 cratons. Subsequent studies using denser arrays covering southeast mainland Australia (Arroucau et al., 2010),
 131 southeastern Australia (Young et al. 2013), and northern Tasmania (Young et al., 2011) show good correlations
 132 between group/phase velocity maps and sedimentary and basement terrane boundaries. In order to account for
 133 uneven data distribution, Bodin et al. (2012b) used a Bayesian transdimensional inversion scheme to generate
 134 group velocity maps that span the Australian continent from multi-scale ambient noise datasets. However, in our
 135 study area their model is of low resolution due to the limited station coverage and hence few details on crustal
 136 structure can be inferred. Bodin et al. (2012a) subsequently applied Bayesian statistics to reconstruct the Moho
 137 geometry of Australia using a variety of seismic datasets, which gave an approximate Moho depth of ~ 30 km
 138 beneath Bass Strait. Pilia et al. (2015a,b) and Crowder et al. (2019) derived 3-D shear wave velocity models of
 139 the Bass strait region using ambient noise data from the same array of temporary stations that we exploit in this
 140 study. They were able to constrain the lateral and depth extent of the primary sedimentary basins in the region,
 141 and provide insight into the seismic character of the Precambrian micro-continental block that appears to
 142 underpin southern Victoria, north western Tasmania and Bass Strait.

143 Teleseismic tomography has also been used to image the lithosphere beneath southeast Australia, thanks in part
 144 to the prolific deployment of short-period seismometers as part of the WOMBAT transportable array project
 145 (Rawlinson and Kennett, 2008, Rawlinson et al., 2015, 2016). While the main focus has been on the upper
 146 mantle, in Tasmania, where station spacing was denser, some constraints on crustal velocity structure were
 147 possible. Rawlinson et al. (2006) found that the crust beneath the ETT was significantly faster than the crust
 148 beneath central Tasmania, which may represent a contrast between crust with oceanic provenance in the east and
 149 Precambrian continental provenance in the west. Bello et al. (2019b) built on this work by including teleseismic
 150 arrival time data from the same temporary deployment as the the current study to generate a detailed upper
 151 mantle model of southeast Australia, which revealed that Bass Strait was underlain by lower velocities,

152 consistent with thinned lithosphere as a result of failed rifting during the break-up of Australia and Antarctica.

153 Active source seismic profiling has also been widely used in southeast Australia to characterize crustal velocity
154 structure (e.g. Finlayson et al., 1980; Collins, 1991; Finlayson et al., 2002; Drummond et al., 2006; Glen, 2013).
155 This has largely focused on the transition from continental to oceanic crust at passive margins, but has also been
156 used to image major transition zones or faults between orogens (Glen, 2013) or within orogens (Cayley et al.,
157 2011a,b), the latter of which lead to the VanDieland microcontinental model. Rawlinson and Urvoy (2006)
158 jointly inverted teleseismic arrival times and active source wide-angle traveltimes in northern Tasmania to
159 constrain crustal velocity, Moho geometry and upper mantle velocity structure and found that both northeastern
160 and northwestern Tasmania is characterised by thinner (<28 km) and higher velocity crust compared to central
161 Tasmania.

162 Potential field data have also been exploited to study the formation and structure of the Tasmanides. Gunn et al.
163 (1997) integrated potential field data (magnetic and gravity), seismic reflection data, outcrop geology and well
164 information to study the crustal structure of the Australian continent. Their study found that the occurrence of
165 tensional stress, oriented NE-SW along basement structures in the Bass Basin, is able to explain the formation of
166 the three major sedimentary basins that overlie dense mafic material, which in turn was formed by mantle
167 decompression processes associated with crustal stretching. From the interpretation of new aeromagnetic data,
168 Morse et al. (2009) delineated the architecture of the Bass Strait basins and their supporting basement structure.
169 Subsequent studies by Moore et al. (2015, 2016) used gravity, magnetic, seismic reflection and outcrop data to
170 support the hypothesis of a VanDieland microcontinent. Their study showed that VanDieland comprises seven
171 distinct microcontinental ribbon terranes that appear to have amalgamated by the Late Cambrian, with major
172 faults and suture zones bonding these ribbon terranes together.

173 While the last few decades have seen important advances and insights made into our understanding of the
174 southern Tasmanides, there still remains limited data on the deep crustal structure beneath Bass Strait, which is
175 our region of interest. It is therefore timely that we can exploit, using the RF technique, teleseismic data
176 recorded by a collection of temporary and permanent seismic stations in the region to study the structure of the
177 crust, Moho and uppermost mantle beneath mainland Australia, Bass Strait and Tasmania.

178 **4 Data**

179 A collaboration involving five organisations (University of Tasmania, Australian National University, Mineral
180 Resources Tasmania, the Geological Survey of Victoria and FROGTECH) deployed the temporary Bass seismic
181 array from May 2011 to April 2013. It consisted of 24 broadband, three-component seismic stations that
182 spanned northern Tasmania, and a selection of islands in Bass Strait and southern Victoria. The instruments
183 used were 23 Güralp 40T and one Güralp 3ESP sensors coupled to Earth Data PR6-24 data loggers. The
184 permanent stations consist of eight broadband sensors managed by IRIS, GEOSCOPE and the Australian
185 National Seismic Network (ANSN). The distribution of all 32 seismic stations that are used in this study is
186 plotted in Figure 2. Earthquakes with magnitudes $m_b > 5.5$ at epicentral distances between 30° and 90° comprise
187 the seismic sources used in this analysis (Fig. 3). This resulted in an acceptable azimuthal coverage of
188 earthquakes between the northwest and east of the array, where active convergence of the Australian and

189 Eurasian plate coupled with westward motion of the Pacific plate has produced extensive subduction zones. To
190 the south and southwest of the array, the absence of subduction zones in the required epicentral distance range
191 means that there are significantly fewer events available for analysis from these regions.

192 **5 Methods**

193 **5.1 Receiver functions**

194 The RF technique (Langston, 1979) uses earthquakes at teleseismic distances to enable estimation of Moho
195 depth and shear wave velocity structure in the vicinity of a seismic recorder. If this technique can be applied to a
196 network of stations with good spatial coverage, it represents an effective way of mapping lateral variations in
197 Moho depth and crustal structure.

198 A recorded teleseismic wavefield at a broadband station can be described by the convolutional model in which
199 operators that represent the source radiation pattern, path effects, crustal structure below the station and
200 instrument response are combined to describe the recorded waveform. By using deconvolution to remove the
201 effects of the source, path and response of the instrument (e.g. Langston, 1979), information on local crustal
202 structure beneath the station can be extracted from *P-S* wave conversions at discontinuities in seismic velocity
203 (Owens et al., 1987; Ammon, 1991).

204 *P*-wave RFs were determined from teleseismic *P*-waveforms using FuncLab software (Eagar and Fouch, 2012;
205 Porritt and Miller, 2018), following preprocessing using the seismic analysis code (SAC) (Goldstein et al.,
206 2003). RFs were computed by applying an iterative time-domain deconvolution scheme developed by Ligorria
207 and Ammon (1999) with a 2.5 s Gaussian filter width. This is achieved by deconvolution of the vertical
208 component waveform from the radial and transverse waveforms with a central frequency of ~ 1 Hz. This
209 frequency was selected on account of significant source energy detected in the ~ 1 Hz range of teleseismic *P*
210 arrivals, which are sensitive to crustal-scale anomalies. It also provides a favourable lateral sensitivity with
211 respect to Fresnel zone width (~ 15 km at Moho depth) when the conversions from *P* to *S* are mapped as
212 velocity and crustal thickness variations.

213 The complete set of 1765 events (Fig. 3) and 32 stations produced 21,671 preliminary RFs. These RFs were
214 manually inspected using the FuncLab trace editor and a subset of 9,674 RFs were selected for further analysis
215 using the visual clarity of the direct arrivals as an acceptance criterion. Due to high noise levels and fewer
216 events associated with the temporary BASS array dataset, a modest number of good quality RFs resulted from
217 the above selection method, so different selection criteria were applied that assessed the *P*-arrival, Moho
218 conversion and later amplitudes in conjunction with overall noise levels exhibited by the transverse component
219 RFs. This enabled the temporary BASS stations to yield between 2 and 30 good quality receiver functions, and
220 increased the number of stations where H- κ stacking and NA inversion could be applied from 13 to 20.

221 **5.2 *H- κ* stacking**

222 Having obtained reliable *P*-wave RFs, the *H- κ* stacking technique is used to estimate crustal thickness and bulk
223 V_p/V_s for individual stations. We apply the method of Zhu and Kanamori (2000) to stations where the direct *Ps*

224 (Moho P -to- S conversion) phase and its multiples are observed. This technique makes use of a grid search to
 225 determine the crustal thickness (H) and V_p/V_s (κ) values that correspond to the peak amplitude of the stacked
 226 phases. A clear maximum requires a contribution from both the primary phase (Ps) and the associated multiples
 227 ($PpPs$ and $PpSs+PsPs$). In the absence of multiples, the maximum becomes smeared out due to the inherent
 228 trade-off between crustal thickness (H) and average crustal velocity properties (κ) (Ammon et al., 1990; Zhu and
 229 Kanamori, 2000). The H - κ stacking algorithm reduces the aforementioned ambiguity by summing RF
 230 amplitudes for Ps and its multiples - $PpPs$ and $PpSs+PsPs$ - at arrival times corresponding to a range of H and
 231 V_p/V_s values. In the H - κ domain the equation for stacking amplitude is

$$232 \quad s(H, \kappa) = \sum_{j=1}^N w_1 r_j(t_1) + w_2 r_j(t_2) + w_3 r_j(t_3) \quad (1)$$

233 where $r_j(t_i)$; $i=1,2,3$ are the RF amplitude values at the expected arrival times t_1 , t_2 , t_3 of the Ps , $PpPs$,
 234 $PpSs+PsPs$ phases respectively for the j^{th} RF, w_1 , w_2 , w_3 are weights based on the signal to noise ratio
 235 ($w_1+w_2+w_3=1$), and N is the total number of radial RFs for the station. $s(H, \kappa)$ achieves its maximum value when
 236 all three phases stack constructively, thereby producing estimates for H and V_p/V_s beneath the station (see
 237 Figure 5 and Supplementary Figures S1-S4). In this study, the weighting factors used are $w_1=0.6$, $w_2=0.3$,
 238 $w_3=0.1$. The H - κ approach requires an estimate of the mean crustal P -wave velocity, which is used as an initial
 239 value. Based on the results of a previous seismic refraction study (Drummond and Collins, 1986), we use an
 240 average crustal velocity of $V_p = 6.65$ km/s to obtain our estimates of H and κ in the study area, noting that H - κ
 241 stacking results are much more dependent on V_p/V_s than V_p (Zhu and Kanamori, 2000). To estimate the
 242 uncertainties in the H - κ stacking results, we compute the standard deviation of the H and κ values at each
 243 station. When only a small number of RFs are available at a station (e.g. 4 in the case of MILA) the estimates
 244 are unlikely to be particularly robust, and in such instances are perhaps best viewed as a lower bounds on
 245 uncertainty.

246 While simple to implement, the Zhu and Kanamori (2000) method can suffer from large uncertainties due to its
 247 assumption of a simple flat-laying layer over a half-space with constant crustal and upper mantle properties.
 248 Consequently, there are only two search parameters (H and κ) plus *a priori* information (V_p , weightings) and it
 249 does not account for variation with backazimuth. These problems can cause non-unique and inaccurate
 250 estimates, which can lead to potentially misleading interpretations; for instance, a low velocity upper crustal
 251 layer can appear as a very shallow Moho in an H - κ stacking search space diagram. Also, a dipping Moho and/or
 252 anisotropic layers within the crust can contribute to uncertainty.

253 **5.3 Nonlinear waveform inversion**

254 In an effort to refine the crustal model, we invert a stack of the radial RFs by adopting the workflow described
 255 by Shibutani et al. (1996). We divide the waveform data (RFs) into four 90° quadrants based on the backazimuth
 256 of their incoming energy. The 1st quadrant backazimuth range is from 0° and 90°, and an equivalent range in a
 257 clockwise direction defines the consecutive quadrants. The 2nd and 3rd quadrants (south-eastern and south-
 258 western backazimuths) have very small numbers of RFs. Data from the 1st and 4th quadrants are of better quality,

259 with the 1st quadrant showing more coherency than the 4th quadrant, which is likely due to the orientation of
 260 surrounding tectonic plate boundaries and hence the pattern of *P*-wave energy radiated towards Australia.
 261 Kennett and Furumura (2008) showed that seismic waves arriving in Australia from the northern azimuths
 262 undergo multiple scattering but low intrinsic attenuation due to heterogeneity in the lower crust and mantle; this
 263 tends to produce prolonged high-frequency coda. An important assumption in our inversion is that we neglect
 264 anisotropy and possible Moho dip, which we assume have a second order influence on the waveforms we use to
 265 constrain 1-D models of the crust and upper mantle.

266 Visual examination of coherency in *P* to *S* conversions allows us to select a subset of RF waveforms for
 267 subsequent stacking. This resulted in groups of mutually coherent waveforms after which a moveout correction
 268 is then applied to remove the kinematic effect of different earthquake distances prior to stacking using a cross-
 269 correlation matrix approach described in Chen et al. (2010) and Tkalčić et al. (2011). Our visual acceptance
 270 criteria yields RFs at only 14 out of the 32 stations used for this study. An example of some stacked RFs is
 271 given in Figure 4.

272 We invert RFs for 1-D seismic velocity structure beneath selected seismic stations using the Neighbourhood
 273 Algorithm or NA (Sambridge, 1999a,b) in order to better understand the internal structure of the crust and the
 274 nature of the transition to the upper mantle. NA makes use of Voronoi cells to help construct a searchable
 275 parameter space, with the aim of preferentially sampling regions of low data misfit. In the inversion process, a
 276 Thomson-Haskell matrix method (Thomson, 1950 and Haskell, 1953) was used to calculate a synthetic radial
 277 RF for a given 1-D (layered) structure. During the inversion, as in Shibutani et al. (1996) and Clitheroe et al.
 278 (2000), each model is described by six layers: a layer of sediment, a basement layer, an upper crust, middle crust
 279 and lower crust, and an underlying mantle layer, all of which feature velocity gradients and potentially, velocity
 280 jumps across boundaries. The inversion involves constraining 24 parameters: *V_s* values at the top and bottom of
 281 each layer, layer thickness and the *V_p/V_s* ratio in each layer (Table 1). The inclusion of *V_p/V_s* ratio as an
 282 unknown primarily aims to accommodate the effects of a sediment layer with limited prior constraints
 283 (Bannister et al., 2003). There are two important controlling parameters required by NA: (1) the number of
 284 models produced per iteration (*n_s*); and (2) the number of neighbourhoods re-sampled per iteration (*n_r*). After a
 285 number of trials we chose the maximum number of iterations to be 5500, with *n_s*=13 and *n_r*=13 for all iterations.
 286 We employ a chi-squared χ^2 metric (see Sambridge 1999a for more details) to compute the misfit function,

287 which is a measure of the inconsistency between the true ϕ_i^{obs} , and predicted, $\phi_i^{pre}(m)$ waveforms for a
 288 given model *m* :

$$289 \quad \chi_v^2(m) = \frac{1}{v} \sum_{i=1}^{N_d} \left(\frac{\phi_i^{obs} - \phi_i^{pre}(m)}{\sigma_i} \right)^2 \quad (2)$$

290 where σ_i represents the noise standard deviation determined from ϕ_i^{obs} , following the method described in
 291 Gouveia and Scales (1998), and *v* represents the number of degrees of freedom (the difference between the

number of observations and the number of parameters being inverted for). Using the above stated parameters, the inversion targets the 1-D structure that produces the best fit between the predicted and observed RF. Figures 7-9 and Supplementary Figures S5-S8 present example results of inversions via density plots of the best 1000 data-fitting *S*-wave velocity models produced by the NA. The optimum data fitting model is plotted in red.

6 Results

6.1 *H-κ* stacking results

Maps of crustal thicknesses and average V_p/V_s from *H-κ* stacking in southeast Australia from 16 stations are shown in Figure 6. At the remaining stations, we could not detect any clear multiples or Moho conversions in the RFs from any direction. A previous study by Chevrot and van der Hilst (2000) has noted that this region is devoid of clear multiples. The crustal thickness for all analysed stations in the study area varies from 23.2 ± 5.0 km (BA02) beneath NW Tasmania to 39.1 ± 0.5 km (CAN) beneath the Lachlan Fold Belt, and the variation strongly correlates with topography. Crust beneath VanDieland (Fig. 6a) is thin in the north (~ 37.5 km) and south (~ 33 km), but appears to be considerably thinner beneath the Victorian and Tasmanian margin of Bass Strait (~ 25 km). The mountainous region of the Lachlan Fold Belt has the deepest Moho at 39.1 ± 0.5 km (CAN) and a corresponding V_p/V_s value of 1.73 ± 0.02 . Crust that is consistently between ~ 31 and 33 km thick lies beneath the East Tasmania Terrane and Eastern Bass Strait (ETT+EB). V_p/V_s ratio varies between ~ 1.65 beneath station BA11, which also exhibits the thinnest crust, and ~ 1.93 beneath stations BA19 and BA20 in southern Victoria. There is no obvious correlation between the number of RFs used in the *H-κ* stacking and the size of the uncertainty in either Moho depth or V_p/V_s , but as mentioned previously, the uncertainty estimates for stations with a low number of RFs are likely to be less robust. Table 2 shows a summary of *H-κ* stacking results for the stations that have been analysed.

6.2 Nonlinear inversion results

Results of the NA inversion were successfully obtained for a selection of permanent and temporary stations, as shown in Table 2 and Figure 10. If the Moho is defined by a gentle velocity gradient, the base of the velocity gradient is used as a proxy for the Moho depth, as done in previous RF (e.g. Clitheroe et al., 2000; Fontaine et al., 2013a) and seismic refraction (Collins, 1991; Collins et al., 2003) studies. We also adopt an upper mantle velocity of $V_p = 7.6$ km/s (i.e. $V_s = 4.3$ - 4.4 km/s for V_p/V_s ratios of 1.73-1.77 at the base of the Moho gradient) following Clitheroe et al. (2000) who used this value for RF studies, and Collins et al. (2003) who used $V_p > 7.8$ km/s for their summary of both seismic refraction and RF results; these V_p values are consistent with global Earth models (e.g. Kennett et al., 1995). Therefore, we also require the *S*-wave velocity to be $> \sim 4.4$ km/s beneath the Moho. We present the *S*-wave velocity profiles from the NA inversion for stations CAN, MOO, TOO, YNG, BA13 and BA17 in Figures 7-9, together with observed and predicted RFs. The *S*-wave velocity inversion results of the remaining stations are included as supplementary material (see Supplementary Figures S5-S8). In assigning the Moho depth, we consider three criteria to examine the quality of the inversion result: (1) misfit value χ^2 ; (2) the quality of the RF stack (which is based on our ability to pick the direct and multiple phases); and (3) the visual fit between the synthetic and observed RF. Models that fail to fit significant arrivals in the observed RF are rejected. Based on these criteria, the inversion results are classified as:

- 329 • Very good: very low χ^2 (typically < 0.4), very good visual fit to direct and multiple phases.
- 330 • Good: low χ^2 (typically 0.4-0.8), direct phases clearly visible, multiple phases less clear, and a good
331 visual fit to all major identifiable phases.
- 332 • Poor: medium to high χ^2 (in the range 0.8-1.2), direct phases visible, multiple phases unclear, and
333 moderate visual fit to some identifiable phases. Looking at the character of the crust-mantle transition,
334 this study classifies the transition zone as sharp ≤ 2 km, intermediate 2-10 km or broad ≥ 10 km as
335 initially proposed by Shibutani et al. (1996) and modified by Clitheroe et al. (2000).

336 In general, the optimum χ^2 value is normally considered to be 1, since below this value, the tendency is to fit
337 noise rather than signal. However, this is for the ideal case when the number of degrees of freedom and the
338 absolute values of the data uncertainty are well known (e.g. in the case of a synthetic test). In the case of
339 observational data, these values are often poorly constrained, so using the relative χ^2 values coupled with visual
340 assessment of the data fit appears to be reasonable.

341 We also note that for the seven permanent stations for which we produce receiver function inversion/H- κ
342 stacking results, five have estimates of Moho depth from previous receiver function studies. Clitheroe et al.,
343 (2000) estimated Moho depth at 49 km beneath CAN based on a non-linear inversion, which is ~ 10 km greater
344 than the results we obtain for both NA inversion and H- κ stacking (see section 7.1 for further discussion of this
345 discrepancy). Ford et al. (2010) determine Moho depth beneath stations MOO, TOO, TAU and YNG using H- κ
346 stacking and find values (compared to our H- κ stacking results) of 33 ± 3 km (33.0 ± 1.2 km), 34 ± 3 km (37.5 ± 1.2
347 km), 32 ± 3 km (33.5 ± 1.9 km) and 33 ± 2 km (37.3 ± 0.5 km) respectively. These are all within error, with the slight
348 exception of station YNG, located in Young, on the western flanks of the Great Dividing Range, where we
349 might expect the crust to be slightly thicker than average. Overall, however, these similarities suggest that our
350 results are likely to be robust.

351 **7 Discussion**

352 For convenience, the seismic stations are separated into three groups (Fig. 2) based on tectonic setting and the
353 results obtained. Stations YNG, CAN, CNB, MILA and BA13 are located in the Lachlan Fold Belt; stations
354 BA02, BA11, BA19, BA20, TAU, MOO and TOO sit above the VanDieland microcontinental block; and
355 stations BA07, BA08, BA09 and BA17 lie in the East Tasmania Terrane and Eastern Bass Strait (ETT+EB).
356 Stations BA22 and BA24 lie to the west of VanDieland. This discussion focuses on crustal thickness, the nature
357 of the Moho and crustal velocity and velocity ratio variations from H- κ stacking and the 1-D S-wave velocity
358 models. Overall, the agreement between Moho depths obtained from the H- κ stacking results and NA-inversion
359 is generally within error (Table 2), which makes a joint interpretation more straight forward. Comparison is also
360 made to other studies that have examined crustal seismic properties in southeast Australia, and we attempt to
361 integrate our new findings with previous results from teleseismic tomography, SKS splitting and ambient noise
362 tomography in order to better understand the crust and upper mantle structure and dynamics beneath this region.

363 **7.1 Lateral variation of crustal thickness and nature of the Moho**

364 The RF analysis clearly reveals the presence of lateral changes in crustal thickness that span mainland Australia
 365 through Bass Strait to Tasmania (Figures 6 and 10; in the latter case, RF depths from previous studies are also
 366 included for reference). The stations located in the Palaeozoic Lachlan Fold Belt reveal a generally thick crust
 367 that ranges between ~37 and 40 km. Although the Moho was picked as a velocity jump for stations YNG, CAN
 368 and CNB, the velocity nonetheless tends to continue to increase with depth below the discontinuity. This,
 369 coupled with the fact that Clitheroe et al. (2000) estimate the Moho to be almost 10 km deeper beneath CAN, is
 370 consistent with the presence of mafic underplating (e.g. Drummond and Collins, 1986; Shibutani et al., 1996;
 371 Clitheroe et al., 2000), sourced from the ambient convecting mantle. The top and bottom of such a layer could
 372 feature a velocity step with depth and its internal structure is likely to be layered and/or gradational, hence
 373 resulting in uncertainty in the true Moho depth. Based on deep crustal reflection profiling, Glen et al. (2002)
 374 suggested that the deep Moho underlying the Lachlan Orogen results from magmatic underplating that added a
 375 thick Ordovician mafic layer at the base of the crust coupled with a thick sequence of Ordovician mafic rocks
 376 that can be found in the mid and lower crust. Finlayson et al. (2002) and Glen et al. (2002) also inferred the
 377 presence of underplating near CNB and CAN from seismic refraction data. Collins (2002) postulated that the
 378 underplating might have occurred in the back-arc region of a subduction zone due to pronounced adiabatic
 379 decompression melting in the asthenosphere. The seismic tomography model of Rawlinson et al. (2010, 2011)
 380 exhibits an increase in *P*-wavespeed at 50 km depth beneath CAN, CNB and YNG and the authors suggest that
 381 magmatic underplating may be the cause of the high velocity anomaly. A recent study by Davies et al. (2015)
 382 identified the longest continental hotspot track in the world (over 2000 km total length), which began in north
 383 Queensland at ~33 Ma, and propagated southward underneath the present-day Lachlan Fold Belt and Bass
 384 Strait. The magmatic underplating could therefore be a consequence of the passage of the continent above a
 385 mantle upwelling leading to a more diffuse crust-mantle transition zone. The thickened crust and a transitional
 386 Moho observed in the Lachlan Fold Belt are consistent with the proposed delamination models of Collins and
 387 Vernon (1994).

388 Strong lateral changes in crustal seismic structure (Figures 6 and 10) beneath VanDieland appear to be a
 389 reflection of the region's complex tectonic history. The thick crust (~37 km) beneath the Selwyn Block (see
 390 Figure 1 for its location) – within the northern margin of VanDieland in southern Victoria – thins dramatically
 391 to ~26 km as it enters Bass Strait, increases to ~30 km beneath King Island (BA11), then thins to ~23 km
 392 beneath NW Tasmania, before increasing to ~33 km in southern Tasmania. The results in southern Tasmania
 393 agree with those of Korsch et al. (2002) from a seismic reflection profile adjacent to the seismic stations TAU
 394 and MOO. The thinner crust beneath Bass Strait and its margins may be a consequence of lithospheric thinning
 395 and/or delamination associated with failed rifting that accompanied the break-up of Australia and Antarctica
 396 (Gaina et al., 1998). Stations BA07, BA08, BA09 and BA17 (ETT+EB) collectively indicate crust of relative
 397 uniform thickness (~31-32 km, Figures 10a,b). Relative to western Bass Strait, the crust is slightly thicker in
 398 this part of the study area, which may suggest underplating associated with a Palaeozoic subduction system (e.g.
 399 Drummond and Collins, 1986; Gray and Foster, 2004).

400 In general, our understanding of crustal thicknesses variations are limited by station separation, so it is difficult
 401 to determine whether smooth variations in thickness or step-like transitions explain the observations.

402 7.2 V_p/V_s and bulk crustal composition

403 V_p/V_s can constrain chemical composition and mineralogy more robustly than P - or S -wave velocity in isolation
404 (Christensen and Fountain, 1975). We observe variations in V_p/V_s across the study region, which we can largely
405 equate with variations in composition or melt. Studies in mineral physics and field observations show (1) a
406 linear increase in Poisson's ratio with decreasing SiO_2 content in the continental crust (Christensen, 1996) and
407 (2) partial melt is revealed by elevated V_p/V_s , especially if the anomaly is localised to an intra-crustal layer
408 (Owens and Zandt, 1997). A more felsic (SiO_2) composition in the lower crust is represented by a lower V_p/V_s ,
409 which reflects removal of an intermediate-mafic zone by delamination, whereas a more mafic lower crust is
410 revealed by higher V_p/V_s (> 1.75) which may be due to underplated material (Pan and Niu, 2011). However,
411 lower crustal delamination can also result in decompression melting, which can yield elevated V_p/V_s (He et al.,
412 2015). We interpret the variation of observed V_p/V_s in the southern Tasmanides to be a consequence of
413 compositionally heterogeneous crust and localised partial melt that may likely be sourced from recent intraplate
414 volcanism (Rawlinson et al., 2017).

415 Figure 6b shows the distribution of bulk V_p/V_s across the study area. The pattern of V_p/V_s ratios appears to
416 delineate three distinct zones of crust. Beneath the Lachlan Orogen, values are ~ 1.75 , which is consistent with
417 the presence of a mafic lower crust, as suggested by a number of other studies (Drummond and Collins, 1986;
418 Shibutani et al., 1996; Clitheroe et al., 2000; Finlayson et al., 2002). Beneath eastern Bass Strait, the V_p/V_s
419 ratios are slightly lower, with BA07, BA08 and BA09 exhibiting values of 1.70, 1.70 and 1.71 respectively.
420 These values are in agreement with constraints from seismic reflection and refraction studies (Finlayson et al.,
421 2002; Collins et al., 2003) and may indicate a felsic to intermediate crustal composition. The geology of
422 Flinders Island, which hosts both BA07 and BA08, is dominated by Devonian granites, which is consistent with
423 this observation. Beneath VanDieland, V_p/V_s is highly variable, with the greatest contrast between BA11
424 (~ 1.65) and BA19/20 (~ 1.93), and BA19/20 and TOO (1.68). BA11 is located on King Island, which is
425 characterised by Precambrian and Devonian granite outcrops, which may help explain the low V_p/V_s . The high
426 V_p/V_s beneath BA19/20 is harder to explain, but could be caused by melt in the crust associated with the Newer
427 Volcanics Province, which sits along the Cosgrove intraplate volcanic track, and last erupted only ~ 4.6 Ka
428 (Rawlinson et al., 2017). The return to lower V_p/V_s beneath TOO over a relatively short distance (~ 100 km) is
429 also difficult to explain, but we note that this region of Victoria is underlain by granite intrusions.

430 In summary, the crust beneath VanDieland exhibits the greatest lateral heterogeneity in V_p/V_s , which likely
431 reflects considerable variations in composition and the presence of melt. This can partially be explained by the
432 tectonic history of the region, which includes failed rifting in Bass Strait accompanied by widespread magma
433 intrusion and granite emplacement, and more recently, the passage of a plume (Rawlinson et al., 2017).
434 Furthermore, Moore et al. (2015) used reflection transects and potential field data to infer that Vandieland is
435 comprised of up to seven continental ribbon terranes that are bounded by major faults and suture zones, which
436 were likely amalgamated by the end of the Proterozoic. Hence, considerable variations in composition and
437 hence V_p/V_s ratio are to be expected.

438 7.3 Moho depth comparison

439 Prior to this study, a variety of seismic methods have been used to constrain Moho depth in southeast Asia,
440 including receiver functions, reflection profiling and wide-angle refraction and refraction experiments. In an
441 effort to combine the results from all of these studies into a single synthesis, Kennett et al., (2011) developed the
442 AusMoho model. This included Moho depth estimates from over 11,000 km of reflection transects across the
443 continent, numerous refraction studies, and 150 portable and temporary stations. Due to irregular sampling, the
444 detail of this model is highly variable; for example, the region beneath Bass Strait is constrained by only five
445 measurements, whereas the central Lachlan Fold Belt around Canberra (see Figure 1 for location) features
446 relatively dense sampling at ~50 km intervals or less.

447 AusMoho includes previous receiver function results from Shibutani et al. (1996), Clitheroe et al. (2000),
448 Fontaine et al. (2013a) and Tkalcic et al (2012), as well as reflection and refraction transects in Tasmania, parts
449 of the Lachlan Orogen, and western Victoria. Figure 11 illustrates AusMoho for our study region, which
450 exhibits large variations in Moho depth (from ~10 km to >50 km). These extremes are due to the presence of
451 oceanic crust outboard of the passive margin of the Australian continent, and the root beneath the Southern
452 Highlands, which represent the southern extension of the Great Dividing Range in New South Wales.
453 Superimposed on Figure 11 are Moho depths from the four previous receiver function studies cited above, plus
454 NA inversion and H- κ depth estimates from this study. As expected, the correlation between the previous RF
455 results and AusMoho is generally good, since they were part of the dataset used to build this model. In places
456 where they don't match, this can be attributed to the presence of seismic refraction or reflection lines which
457 were also used to constrain AusMoho.

458 In general, the agreement between the results from this study and AusMoho is good, but there are exceptions.
459 For instance, CAN, CNB, YNG and MILA tend to be somewhat shallower than AusMoho. However, this can be
460 attributed to the likely presence of mafic underplating alluded to earlier, which can effectively yield two options
461 for the Moho transition due to an expected high (>1.85) V_p/V_s in the underplate layer (e.g. Cornwell et al.,
462 2010). AusMoho Moho depths beneath BA07 and BA08 are considerably shallower than our estimates, which
463 we attribute to a lack of data coverage in this region. Sizeable discrepancies also exist beneath BA02, BA19 and
464 BA20; in the former case, the uncertainty in our H- κ stacking estimate is 5 km, which may be a factor here. In
465 the latter case, we also note that there is sparse data coverage southeast of Melbourne to constrain AusMoho, so
466 it would appear that our new Moho depths are more likely to be correct. Overall, while there is good consistency
467 between AusMoho and our new results, any updated version of AusMoho should incorporate the Moho depth
468 estimates from this study.

469 Although AusMoho did make use of results from a 3-D wide-angle reflection and refraction survey of Tasmania
470 (offshore shots and on-shore stations), it only used a few sample points for the final Moho model (Kennett et al.,
471 2011), and therefore the resolution of AusMoho is considerably less than the Moho model produced by
472 Rawlinson et al. (2001). Consequently, we plot our three RF results on top of this model in Supplementary
473 Figure S9. The agreement between the Moho model and RF depths beneath MOO and TAU is good, but RF
474 estimates beneath BA02 are shallower than the Moho model by about 4 km. However, this is within the margin
475 of error for the H- κ stacking result.

476 7.4 Synthesis

477 In this final section, we present a synthesis of results for southeast Australia that are based on: (1) our new
 478 receiver function results; (2) teleseismic SKS splitting results from Bello et al. (2019a); (3) teleseismic
 479 tomography undertaken by Bello et al. (2019b); (4) ambient noise crustal imaging results from Young et al.
 480 (2013); and (5) AusMoho (Kennett et al., 2011). This synthesis is encapsulated in the plot shown in Figure 12,
 481 which is a representative transect through the Lachlan Orogen south through Bass Strait and into Tasmania.
 482 Moho depths are taken from AusMoho, and refined where additional information is available from our new RF
 483 results; crustal P-wave velocity is taken from the ambient noise results (following conversion from *S*-wave
 484 velocity – see Bello et al, 2019b for more details); and mantle *P*-wave velocities are taken from Bello et al,
 485 (2019b). Arrows are based on interpreted mantle flow patterns undertaken as part of the shear wave splitting
 486 study. This previous study used approximately the same temporary and broadband station network that was used
 487 in the current study, and found that beneath the Lachlan Orogen, fast axis orientations of anisotropy were
 488 aligned with contemporary plate motion (NNE), but beneath Bass Strait, a radial pattern was observed that is
 489 consistent with an upwelling mantle that impinges on the lithosphere and spreads out in all directions.
 490 Interestingly, the location of this phenomenon corresponds approximately to the predicted location of the
 491 Cosgrove hotspot track source (Davies et al., 2015), and may be caused by an upwelling mantle plume. Thus,
 492 the low velocities in the upper mantle beneath Bass Strait may be due to elevated temperatures and melt,
 493 although it is not straightforward to explain the higher velocities below 200 km depth in this context.

494 The thicker Moho boundary beneath the Lachlan Orogen (Figure 12) reflects the likely presence of
 495 underplating, which makes the base of the crust harder to discern seismically. However, the crust is clearly
 496 thicker here than beneath Bass Strait or Tasmania. Moho depth beneath the northern part of the Figure 12 is not
 497 constrained by our RF results, but according to AusMoho, it is relatively flat, which is consistent with
 498 Precambrian crust, and there is a faster mantle lithosphere. The strong variations in crustal velocity beneath Bass
 499 Strait can be attributed to failed rifting resulting in the formation of thick (>10 km) sedimentary basins and
 500 elevated temperatures (lower velocities), and intrusion of mafic rich material into the lower and mid crust
 501 (higher velocities).

502 **8 Conclusions**

503 We used *H-κ* stacking of teleseismic RFs to determine crustal thickness and V_p/V_s ratio and generate 1-D *S*-
 504 wave velocity profiles of the crust from RF inversion in order to investigate the internal crustal velocity
 505 structure beneath the southern Tasmanides in southeast Australia. Our main findings are summarised below.

- 506 • The thick crust and broad crust-mantle transition beneath the Lachlan Fold Belt may be caused by
 507 magmatic underplating of mafic materials beneath the crust, which is consistent with an elevated V_p/V_s
 508 ratio (relative to ak135) of ~ 1.73 . Thicker crust is also to be expected from the elevated topography of
 509 the eastern Lachlan Fold Belt.
- 510 • The crustal structure is complex beneath VanDieland. It thins considerably from the northern tip of the
 511 microcontinent (~ 37 km) into Bass Strait (~ 26 km) and northern Tasmania (~ 23 km), yet in southern
 512 Tasmania the crust is somewhat thicker (~ 33 km) compared to Bass Strait. This may in part be due to
 513 the complex origins of the microcontinent, which appears to be comprised of multiple Precambrian

continental ribbons, but is also likely due to failed rifting in Bass Strait before and during the separation of Australia and Antarctica. This resulted in lithospheric stretching/delamination, magmatic intrusion, and the deposition of thick sedimentary sequences. Recent intraplate volcanism and the possible progression of a mantle plume beneath Vandieland in the last few thousand years may also have produced compositional heterogeneity and melt in the crust. Such events are likely to contribute significantly to variations in crustal thickness and the pronounced changes in V_p/V_s that we observe.

- Stations within the ETT+EB collectively indicate crust of uniform thickness ($\sim 31\text{--}32$ km) and uniform V_p/V_s (~ 1.70), which clearly distinguishes it from Vandieland. This region of the crust likely represents a southern continuation of the Lachlan Orogen, and therefore is underpinned by crust of oceanic origin.

- Comparison of our new Moho depth results with the AusMoho model reveals an overall consistency, although at some of our station locations where AusMoho has few constraints, there are noticeable differences, such as southern Victoria and beneath Flinders Island. The discrepancies beneath the Lachlan Orogen are attributed to the presence of underplated mafic material, which can obfuscate the location of the Moho.

- A synthesis of our new RF results with pre-existing teleseismic tomography, shear wave splitting and ambient noise studies reveals a complex lithosphere that has clearly been impacted by orogeny (thickened crust), failed rifting beneath Bass Strait (thinned crust and complex crustal velocities), and recent intraplate volcanism (high V_p/V_s ratios and a radial pattern of fast anisotropy patterns above a presumed zone of mantle upwelling).

9 Data availability

Dataset available at [10.6084/m9.figshare.12233723](https://doi.org/10.6084/m9.figshare.12233723)

10 Author contributions

M.B. performed the data analysis and wrote the draft manuscript. N.R and D.C. guided the study and assisted in interpretation. M.B., D.C. and N.R. discussed the results and revised the manuscript. A.R. and O.L. revised the manuscript and assisted with the interpretation.

11 Competing Interests: The authors declare no competing interests.

12 Acknowledgments

The work in this paper was performed as part of a PhD study and has been jointly funded by Abubakar Tafawa Balewa University (ATBU), Bauchi, Nigeria and the University of Aberdeen, UK. The authors acknowledge the efforts of staff, students and fieldwork technicians from the Australian National University and University of Tasmania, who deployed the temporary BASS array used in this study. We also thank Qi Li and Armando

545 Arcidiaco for their efforts in BASS data pre-processing and archiving. Australian Research Council Grant
 546 LP110100256 supported the BASS deployment. We are grateful to IRIS and Geoscience Australia for providing
 547 data from several stations in mainland Australia and Tasmania. Figure 1 was made using Inkscape software
 548 (Harrington, et. al., 2005) and Figures 2, 3, 6 and 9 were produced using the Generic Mapping Tools (Wessel et
 549 al., 2013).

550 **References**

- 551 Amante, C. and Eakins, B. W.: ETOPO1 1 Arc-Minute Global Relief Model: Procedures, data sources and
 552 analysis, NOAA technical memorandum NESDIS NGDC-24, 19pp, 2009.
- 553 Ammon, C. J.: The isolation of receiver effects from teleseismic P waveforms. *Bull. Seis. Soc. Ame.*, 81, 2504–
 554 2510, 1991.
- 555 Ammon, C. J., Randall, G., and Zandt, G.: On the nonuniqueness of receiver function inversions. *J. Geophys.*
 556 *Res.*, 95, 15 303–15 318, 1990.
- 557 Arroucau, P., Rawlinson, N., and Sambridge, M.: New insight into Cainozoic sedimentary basins and
 558 Palaeozoic suture zones in southeast Australia from ambient noise surface wave tomography. *Geophys. Res.*
 559 *Lett.*, 37, <http://dx.doi.org/10.1029/2009GL041974>, 2010.
- 560 Bannister, S., Yu, J., Leitner, B., and Kennett, B. L. N.: Variations in crustal structure across the transition from
 561 West to East Antarctica, Southern Victoria Land, *Geophys. J. Int.*, 155, 870–884, 2003.
- 562 Bello, M., Cornwell, D. G., Rawlinson, N., and Reading, A. M.: Insights into the structure and dynamics of the
 563 upper mantle beneath Bass Strait, southeast Australia, using shear wave splitting, *Phys. Earth Planet. Inter.*,
 564 289, 45–62, <https://doi.org/10.1016/j.pepi.2019.02.002>, 2019a.
- 565 Bello, M., Rawlinson, N., Cornwell, D. G., Crowder, E., Salmon, M., and Reading, A. M.: Structure of the crust
 566 and upper mantle beneath Bass Strait, southeast Australia, from teleseismic body wave tomography, *Phys.*
 567 *Earth Planet. Inter.*, 294, <https://doi.org/10.1016/j.pepi.2019.106276>, 2019b.
- 568 Berry, R. F., Steele, D. A., and Maffre, S.: Proterozoic metamorphism in Tasmania: implications for tectonic
 569 reconstructions, *Prec. Res.*, 166, 387–396. <https://doi.org/10.1016/j.precamres.2007.05.004>, 2008.
- 570 Bodin, T., Salmon, M., Kennett, B. L. N., and Sambridge, M.: Probabilistic surface reconstruction from multiple
 571 datasets: an example for the Australian Moho, *J. Geophys. Res.: Solid Earth*, 117,
 572 <http://dx.doi.org/10.1029/2012JB009547>, 2012a.
- 573 Bodin, T., Sambridge, M., Rawlinson, N., and Arroucau, P.: Transdimensional tomography with unknown data
 574 noise, *Geophys. J. Int.*, 189, 1536–1556, 2012b.
- 575 Boger, S. and Miller, J.: Terminal suturing of Gondwana and the onset of the Ross Delamerian Orogeny: the
 576 cause and effect of an Early Cambrian reconfiguration of plate motions, *Earth Planet. Sci. Lett.*, 219, 35–48,
 577 2004.
- 578 Calvert, C. R. and Walter, M. R.: The Late Neoproterozoic Grassy Group of King Island, Tasmania: correlation
 579 and palaeogeographic significance, *Precam. Res.*, 100, 299–312, 2000.
- 580 Cawood, P. A.: Terra Australis Orogen: Rodinia breakup and development of the Pacific and Iapetus margins of
 581 Gondwana during the Neoproterozoic and Palaeozoic. *Earth-Science Reviews*, 69, 249–279,
 582 <http://dx.doi.org/10.1016/j.earscirev.2004.09.001>, 2005.
- 583 Cayley, R.: Exotic crustal block accretion to the eastern Gondwanaland margin in the Late Cambrian Tasmania,
 584 the Selwyn Block, and implications for the Cambrian–Silurian evolution of the Ross, Delamerian, and
 585 Lachlan orogens. *Gond. Res.*, 19, 628–649. <http://dx.doi.org/10.1016/j.gr.2010.11.013>, 2011a.

586 Cayley, R., Korsch, R. J., Moore, D. H., Costelloe, R. D., Nakamura, A., Willman, C. E., Rawlin, T. J., Morand,
587 V. J., Skladzien, P. B., and O'Shea, P. J.: Crustal architecture of central Victoria: results from the 2006 deep
588 crustal reflection seismic survey, *Aust. J. Earth Sci.*, 59, 113–156, 2011b.

589 Chen, Y., Niu, F., Liu, R., Huang, Z., Tkalčić, H., Sun, L., and Chan, W.: Crustal structure beneath China from
590 receiver function analysis, *J. Geophys. Res.*, 49(B033067), 2010.

591 Chevrot, S. and van der Hilst, R. D.: The Poisson ratio of the Australian crust: Geological and Geophysical
592 implications, *Earth Planet. Sci. Lett.*, 183, 121–132, 2000.

593 Christensen, N. I.: Poisson's ratio and crustal seismology, *J. Geophys. Res.*, 101, 3139–3156, 1996.

594 Christensen, N. I. and Fountain, D. M.: Constitution of the lower continental crust based on experimental studies
595 of seismic velocities in granulite, *Geol. Soc. Ame. Bull.*, 86, 227–236, 1975.

596 Clitheroe, G., Gudmundsson, O., and Kennett, B.: The crustal thickness of Australia, *J. Geophys. Res.*, 105, 13
597 697–13 713, 2000.

598 Collins, C. D. N.: The nature of crust–mantle boundary under Australia from seismic evidence, In: Drummond
599 B. J. ed. *The Australian lithosphere*, *Geol. Soc. Aust. Spec. Pub.*, 17, 67–80, 1991.

600 Collins, C. D. N., Drummond, B. J., and Nicoll, M. G.: Crustal thickness patterns in the Australian continent,
601 *Geol. Soc. Ame. Spec. Papers*, 372, 121–128, 2003.

602 Collins, W. J.: Nature of extensional accretionary origins, *Tectonics*, 21, 1024–1036, 2002.

603 Collins, W. J. and Vernon, R. H.: A rift–drift–delamination model of continental evolution: Palaeozoic tectonic
604 development of eastern Australia, *Tectonophysics*, 2(35), 1994.

605 Coney, P. J.: Plate tectonics and the Precambrian Phanerozoic evolution of Australia, PACRIM '95, *Aust. Inst.*
606 *Mining and Metallurgy*, pages 145–150, 1995.

607 Coney, P. J., Edwards, A., Hine, R., Morrison, F., and Windrim, D.: The regional tectonics of the Tasman
608 orogenic system, eastern Australia, *J. Struct. Geol.*, 12(5/6), 519–543, 1990.

609 Cornwell, D. G., P. K. H. Maguire, R. W. England, and G. W. Stuart (2010), Imaging detailed crustal structure
610 and magmatic intrusion across the Ethiopian Rift using a dense linear broadband array, *Geochem. Geophys.*
611 *Geosyst.*, 11, Q0AB03, doi:[10.1029/2009GC002637](https://doi.org/10.1029/2009GC002637).

612 Crowder, E., Rawlinson, N., Pilia, S., Cornwell, D. G., and Reading, A. M.: Transdimensional ambient noise
613 tomography of Bass Strait, southeast Australia, reveals the sedimentary basin and deep crustal structure
614 beneath a failed continental rift, *Geophys. J. Int.*, 217, 970–987, 2019.

615 Davies, D. R., Rawlinson, N., Iaffaldano, N., and Campbell, I. H.: Lithospheric controls on magma composition
616 along Earth's longest continental hotspot track, *Nature*, 525, 511–514, 2015.

617 Drummond, B. J. and Collins, C. D. N.: Seismic evidence for underplating of the lower continental crust of
618 Australia, *Earth Planet. Sci. Lett.*, 79, 361–372, 1986.

619 Drummond, B. J., Lyons, P., Goleby, B., and Jones, L.: Constraining models of the tectonic setting of the giant
620 Olympic Dam iron-oxide-copper-gold deposit, south Australia, using deep seismic reflection data,
621 *Tectonophysics*, 420, 91–103, 2006.

622 Eagar, K. C. and Fouch, M. J.: FuncLab: A MATLAB interactive toolbox for handling receiver function
623 datasets, *Seismo. Res. Lett.*, <https://doi.org/10.1785/gssrl.83.3.596>, 2012.

624 Finlayson, D. M., Collins, C. D. N., and Denham, D.: Crustal structure under the Lachlan Fold Belt,
625 southeastern Australia, *Phys. Earth Planet. Int.*, 21, 321–342, 1980.

- 626 Finlayson, D. M., Korsch, R. J., Glen, R. A., Leven, J. H., and Johnstone, D. W.: Seismic imaging and crustal
627 architecture across the Lachlan transverse zone, a crosscutting feature of eastern Australia, *Aust. J. Earth*
628 *Sci.*, 49, 311–321, 2002.
- 629 Fishwick, S. and Rawlinson, N.: 3–D structure of the Australian lithosphere from evolving seismic datasets,
630 *Aust. J. Earth Sci.*, 59, 809–826, 2012.
- 631 Foden, J., Elburg, M. A., Dougherty-Page, J., and Burt, A.: The timing and duration of the Delamerian
632 Orogeny: correlation with the Ross Orogen and implications for Gondwana assembly, *J. Geology*, 114, 189–
633 210, 2006.
- 634 Fontaine, F. R., Tkalčić, H., and Kennett, B. L. N.: Crustal complexity in the Lachlan Orogen revealed from
635 teleseismic receiver functions, *Aust. J. Earth Sci.*, 60, 413–430, 2013a.
- 636 Fontaine, F. R., Tkalčić, H., and Kennett, B. L. N.: Imaging crustal structure variation across southeastern
637 Australia, *Tectonophysics*, 582, 112–125, 2013b.
- 638 Foster, D. A. and Gray, D. R.: Evolution and structure of the Lachlan Fold Belt (Orogen) of eastern Australia,
639 *Annu. Rev. Earth Planet. Sci.*, 28, 47–80, 2000.
- 640 Gaina, C., Müller, D., Royer, J. Y., Stock, J., Hardebeck, J., and Symonds, P.: The tectonic history of the
641 Tasman Sea, a puzzle with 13 pieces, *J. Geophys. Res.*, 103, 12,413–12,433, 1998.
- 642 Gibson, G. M., Morse, M. P., Ireland, T. R., and Nayak, G. K.: Arc-continent collision and orogenesis in
643 western Tasmanides: insights from reactivated basement structures and formation of an ocean-continent
644 transform boundary off western Tasmania, *Gondwana Res.*, 19, 608–627, 2011.
- 645 Glen, R. A.: The Tasmanides of Eastern Australia. In: Vaughan, A. P. M., Leat, P. T., Pankhurst, R. J. (Eds.),
646 *Terrane Processes at the Margins of Gondwana*, Geological Society, pages 23–96, 2005.
- 647 Glen, R. A.: Refining accretionary orogen models for the Tasmanides of eastern Australia, *Aust. J. Earth Sci.*,
648 60, 315–370, 2013.
- 649 Glen, R. A., Korsch, R. J., Direen, N. G., Jones, L. E. A., Johnstone, D. W., Lawrie, K. C., Finlayson, D. M.,
650 and Shaw, R. D.: Crustal structure of the Ordovician Macquarie Arc, eastern Lachlan Orogen, based on
651 seismic–reflection profiling, *Aust. J. Earth Sci.*, 49, 323–348, 2002.
- 652 Glen, R. A., Percival, I. G., and Quinn, C. D.: Ordovician continental margin terranes in the Lachlan Orogen,
653 Australia: implications for tectonics in an accretionary orogen along the east Gondwana margin, *Tectonics*,
654 28, <https://doi.org/10.1029/2009TC002446>, 2009.
- 655 Goldstein, P., Dodge, D., Firpo, M., and Minner, L.: SAC2000: Signal processing and analysis tools for
656 seismologists and engineers. Lee, W. H. K. and Kanamori, H. and Jennings, P. C. and Kisslinger, C. (Eds.).
657 In *IASPEI International Handbook of Earthquake and Engineering Seismology*, Academic Press, London,
658 2003.
- 659 Gouveia, W. P. and Scales, J. A.: Bayesian seismic waveform inversion: Parameter estimation and uncertainty
660 analysis, *J. Geophys. Res.*, 103, 2759–2779, 1998.
- 661 Gray, D. R. and Foster, D. A.: Tectonic evolution of the Lachlan Orogen, southeastern Australia: historical
662 review, data synthesis and modern perspectives, *Aust. J. Earth Sci.*, 51, 773–817, 2004.
- 663 Gunn, P. J., Maidment, D. W., and Milligan, P.: Interpreting aeromagnetic data in areas of limited outcrop,
664 *AGSO J. Aust. Geol. Geophys.*, 17, 175–185, 1997.
- 665 Harrington, B. et al (2004–2005). Inkscape. <http://www.inkscape.org/>.
- 666 Haskell, N. A.: The dispersion of surface waves in multilayered media, *Bulletin of the Seismological Society*
667 *America*, 43, 1734, <http://dx.doi.org/10.1038/physci245109a0>, 1953.

668 He, C. S., Santosh, M., Dong, S. W., and Wang, S. C.: Crustal thickening and uplift of the Tibetan Plateau
669 inferred from receiver function analysis, *J. Asian Earth Sci.*, 99, 112–124, 2015.

670 Heintz, M. and Kennett, B. L. N.: Continental scale shear wave splitting analysis: Investigation of seismic
671 anisotropy underneath the Australian continent, *Earth Planet. Sci. Lett.*, 236, 106–119, 2005.

672 Kennett, B. L. N., Engdhal, E. R., and Buland, R.: Constraints on seismic velocities in the earth from travel
673 times. *Geophys. J. Int.*, 125, 228–248, 1995.

674 Kennett, B. L. N. and Furumura, T.: Stochastic waveguide in the lithosphere: Indonesian subduction zone to
675 Australian craton, *Geophys. J. Int.*, 172, 363–382, 2008.

676 Kennett, B. L. N., Salmon, M., Saygin, E., and Group, A.: AusMoho: the variation of Moho depth in Australia,
677 *Geophys. J. Int.*, 187, 946–958, 2011.

678 Korsch, R. J., Barton, T. J., Gray, D. R., Owen, A. J., and Foster, D. A.: Geological interpretation of a deep
679 seismic reflection transect across the boundary between the Delamerian and Lachlan Orogens, in the vicinity
680 of the Grampians, western Victoria, *Aust. J. Earth Sci.*, 49, 1057–1075, <http://dx.doi.org/10.1046/j.1440-0952.2002.00963.x>, 2002.

682 Langston, C. A.: Structure under Mount Rainier, Washington, inferred from teleseismic body waves, *J.*
683 *Geophys. Res.*, 84, 4749–4762, <https://doi.org/10.1071/EG994019>, 1979.

684 Li, Z. X., Baillie, P. W., and Powell, C. M.: Relationship between northwestern Tasmania and East
685 Gondwanaland in the Late Cambrian/Early Ordovician Paleomagnetic evidence, *Tectonics*, 16, 161–171,
686 <http://dx.doi.org/10.1029/96TC02729>, 1997.

687 Ligorria, J. P. and Ammon, C. J.: Iterative deconvolution and receiver function estimation, *Bull. Seism. Soc.*
688 *Ame.*, 89, 1395–1400, 1999.

689 Moore, D., Betts, P. G., and Hall, M.: Fragmented Tasmania: the transition from Rodinia to Gondwana, *Aust. J.*
690 *Earth Sci.*, 62, 1–35, 2015.

691 Moore, D. H., Betts, P. G., and Hall, M.: Constraining the VanDieland microcontinent at the edge of East
692 Gondwana, Australia, *Tectonophysics*, 687, 158–179, 2016.

693 Moresi, L., Betts, P. G., Miller, M. S., and Cayley, R. A.: Dynamics of continental accretion, *Nature*, 508, 245–
694 248, 2014.

695 Morse, M., Gibson, G., and Mitchell, C.: Basement constraints on offshore basin architecture as determined by
696 new aeromagnetic data acquired over Bass Strait and western margin of Tasmania, *ASEG Extended*
697 *Abstracts 2009*, pages 1–9, <http://dx.doi.org/10.1071/ASEG2009ab042>, 2009.

698 Owens, T. J., Taylor, S. R., and Zandt, G.: Crustal structure at regional seismic test network stations determined
699 from inversion of broadband teleseismic P waveforms, *Bull. Seismo. Soc. Ame.*, 77, 631–632, 1987.

700 Owens, T. J. and Zandt, G.: Implications of crustal property with variations for models of Tibetan Plateau
701 evolution, *Nature*, 387, 37–43, 1997.

702 Pan, S. Z. and Niu, F. L.: Large contrasts in crustal structure and composition between the Ordos plateau and the
703 NE Tibetan plateau from receiver function analysis, *Earth Plan. Sci. Lett.*, 303, 291–298, 2011.

704 Pilia, S., Arroucau, P., Rawlinson, N., Reading, A. M., and Cayley, R. A.: Inherited crustal deformation along
705 the East Gondwana margin revealed by seismic anisotropy tomography, *Geophys. Res. Lett.*, 43(23), 12082–
706 12090, <https://doi.org/10.1002/2016GL071201>, 2016.

707 Pilia, S., Rawlinson, N., Cayley, R. A., Musgrave, R., Reading, A. M., Direen, N. G., and Young, M. K.:
708 Evidence of micro-continent entrainment during crustal accretion, *Sci. Rep.*, 5,
709 <http://dx.doi.org/10.1038/srep/08218>, 2015a.

- 710 Pilia, S., Rawlinson, N., Green, N. G., Reading, A. M., Cayley, R., Pryer, L., Arroucau, P., and Duffet, M.:
 711 Linking mainland Australia and Tasmania using ambient seismic noise tomography: Implications for the
 712 tectonic evolution of the east Gondwana margin, *Gond. Res.*, 28, 1212–1227, 2015b.
- 713 Porritt, S. W. and Miller, M. S.: Updates to FuncLab, a Matlab based GUI for handling receiver functions,
 714 *Computers and Geosciences*, 111, 260–271, <https://doi.org/10.1016/j.cageo.2017.11.022>, 2018.
- 715 Rawlinson, N., Davies, D. R., and Pilia, S.: The mechanisms underpinning Cenozoic intraplate volcanism in
 716 eastern Australia, Insights from seismic tomography and geodynamic modeling, *Geophys. Res. Lett.*, 44(19),
 717 9,681–9,690, 2017.
- 718 Rawlinson, N., Housman, G. A., Collins, C. D. N., and Drummond, B. J.: New evidence of Tasmania’s tectonic
 719 history from a novel seismic experiment, *Geophys. Res. Lett.*, 28, 3337–3340, 2001.
- 720 Rawlinson, N. and Kennett, B.: Teleseismic tomography of the upper mantle beneath the southern Lachlan
 721 Orogen, Australia, *Phys. Earth Planet. Inter.*, 167, 84–97, <http://dx.doi.org/10.1016/j.pepi.2008.02.07>, 2008.
- 722 Rawlinson, N., Kennett, B., Vanacore, E., Glen, R., and Fishwick, S.: The structure of the upper mantle beneath
 723 the Delamerian and Lachlan orogens from simultaneous inversion of multiple teleseismic datasets, *Gond.*
 724 *Res.*, 19, 788–799, 2011.
- 725 Rawlinson, N., Kennett, B. L. N., Salmon, M., and Glen, R. A.: Origin of lateral heterogeneities in the upper
 726 mantle beneath Southeast Australia from seismic tomography, Khan, A., and Deschamps, F. (Eds.), In *The*
 727 *Earth’s Heterogeneous Mantle: A Geophysical, Geodynamical and Geochemical Perspective*, pages 47–78,
 728 Springer Geophysics, Springer, 2015.
- 729 Rawlinson, N., Pilia, S., Young, M., Salmon, M., and Yang, Y.: Crust and upper mantle structure beneath
 730 southeast Australia from ambient noise and teleseismic tomography, *Tectonophysics*, 689, 143–156,
 731 <http://dx.doi.org/10.1016/j.tecto.2015.11.034>, 2016.
- 732 Rawlinson, N., Pozgay, S., and Fishwick, S.: Seismic tomography: a window into deep Earth, *Phys. Earth*
 733 *Planet. Inter.*, 178, 101–135, 2010.
- 734 Rawlinson, N. and Urvoy, M.: Simultaneous inversion of active and passive source datasets for 3–D seismic
 735 structure with application to Tasmania, *Geophys. Res. Lett.*, 33, 2006.
- 736 Sambridge, M. S.: Geophysical inversion with a neighbourhood algorithm – I. Searching a parameter space,
 737 *Geophys. J. Int.*, 138, 479–494, 1999a.
- 738 Sambridge, M. S.: Geophysical inversion with a neighbourhood algorithm -II. Appraising the ensemble,
 739 *Geophys. J. Int.*, 138, 479–494, 1999b.
- 740 Saygin, E. and Kennett, B. L. N.: Ambient seismic noise tomography of Australian continent, *Tectonophysics*,
 741 481, 116–125, <http://dx.doi.org/10.1016/j.tecto.2008.11.013>, 2010.
- 742 Shibutani, T., Sambridge, M. S., and Kennett, B. L. N.: Genetic algorithm inversion for receiver functions with
 743 application to crust and uppermost mantle structure beneath Eastern Australia, *Geophys. Res. Lett.*,
 744 23, 1826–1832, 1996.
- 745 Spaggiari, C. V., Gray, D. R., and Foster, D. A.: Lachlan Orogen subduction–accretion systematics revisited,
 746 *Aust. J. of Earth Sci.*, 51, 549–553, 2004.
- 747 Spaggiari, C. V., Gray, D. R., Foster, D. A., and McKnight, S.: Evolution of the boundary between the western
 748 and central Lachlan Orogen: implications for Tasmanide tectonics, *Aust. J. Earth Sci.*, 50, 725–749, 2003.
- 749 Teasdale, J., Pryer, L., Stuart-Smith, P., Romine, K., Etheridge, M., Loutit, T., and Kyan, D.: Structural
 750 framework and basin evolution of Australia’s Southern Margin, *APPEA J. Australian Petroleum Production*
 751 *and Exploration Association*, 43, 13–38, <https://doi.org/10.1785/0120030123>, 2003.

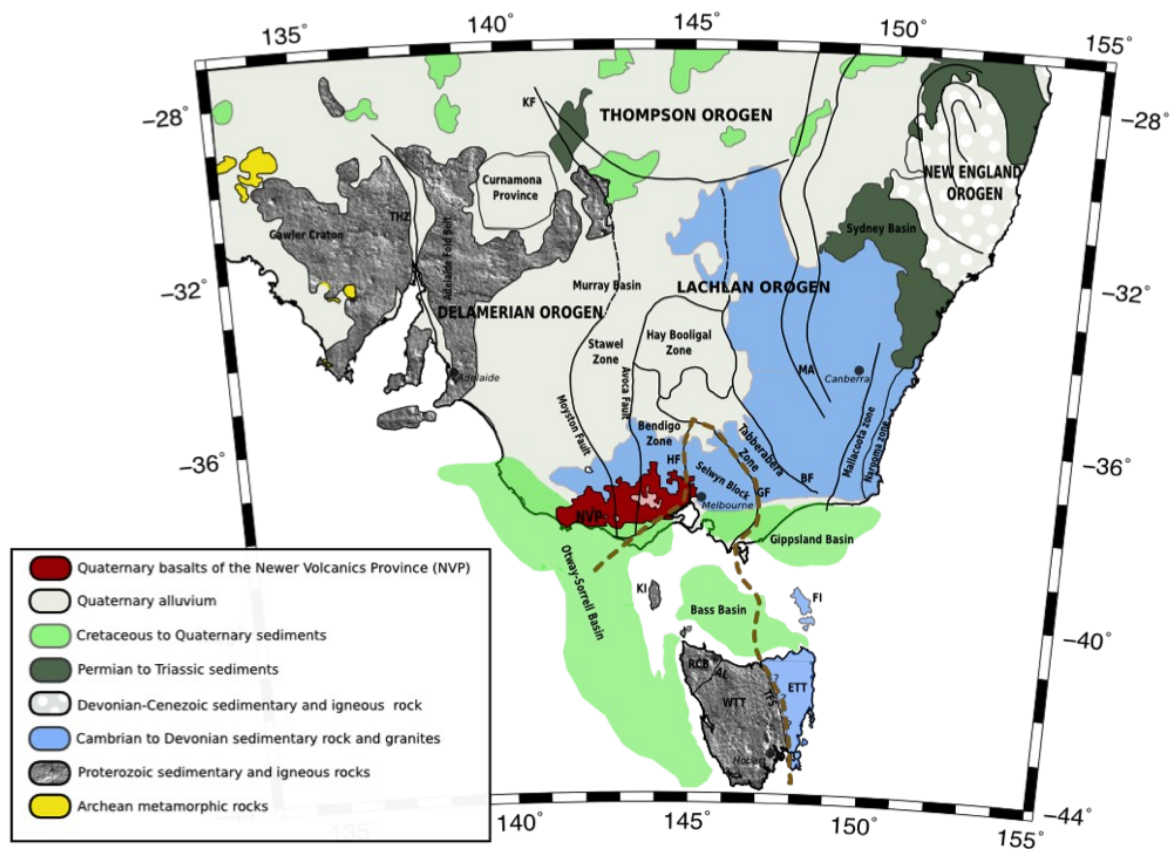
- 752 Thomson, W. T.: Transmission of elastic waves through a stratified solid, *J. of App. Phys.*, 21, 89-93, 1950.
- 753 Tkalčić, H., Chen, Y., Liu, R., Huang, H., Sun, L., and Chan, W.: Multi-step modelling of teleseismic receiver
 754 functions combined with constraints from seismic tomography: Crustal structure beneath southeast China,
 755 *Geophys. J. Int.*, 187, 303–326, 2011.
- 756 Tkalčić, H., Rawlinson, N., Arroucau, P., and Kumar, A.: Multistep modelling of receiver-based seismic and
 757 ambient noise data from WOMBAT array: crustal structure beneath southeast Australia, *Geophys. J. Int.*,
 758 189, 1681–1700, <https://doi.org/10.1111/j.1365-246X.2012.05442>, 2012.
- 759 Wessel, P., Smith, W. H., Scharroo, R., Louis, J., and Wobbe, F.: Generic mapping tools: improved version
 760 released, *EOS Trans. Am. Geophys. Union*, 94, 409-420, 2013.
- 761 Young, M. K., Cayley, R. A., McLean, M. A., Rawlinson, N., Arroucau, P., and Salmon, M.: Crustal structure
 762 of the east Gondwana margin in southeast Australia revealed by transdimensional ambient seismic noise
 763 tomography, *Geophys. Res. Lett.*, 40, 4266–4271, 2013.
- 764 Young, M. K., Rawlinson, N., Arroucau, P., Reading, A., and Tkalčić, H.: High-frequency ambient noise
 765 tomography of southeast Australia: new constraints on Tasmania's tectonic past, *Geophys. Res. Lett.*, 38,
 766 <http://dx.doi.org/10.1029/2011GL047971>, 2011.
- 767 Young, N., Tkalčić, H., Rawlinson, N., and Reading, A. M.: Full waveform moment tensor inversion in a low
 768 seismicity region using multiple teleseismic datasets and ambient noise: application to the 2007 Shark Bay,
 769 Western Australia, *Earthquake. Geophys. J. Int.*, 188, 1303–1321, [https://doi.org/10.1111/j.1365-](https://doi.org/10.1111/j.1365-246X.2011.05326)
 770 [246X.2011.05326](https://doi.org/10.1111/j.1365-246X.2011.05326), 2012.
- 771 Zhu, L. and Kanamori, H.: Moho depth variation in southern California from teleseismic receiver functions, *J.*
 772 *Geophys. Res.*, 105, 2969–2980, 2000.

Table 1: Model parameter bounds used in the Neighbourhood Algorithm receiver function inversion. V_s^{upper} and V_s^{lower} represent the S -velocity at the top and bottom of a layer respectively. V_p/V_s represents P and S wave velocity ratio within a layer.

Layer	Thickness (m)	V_s^{upper} (km/s)	V_s^{lower} (km/s)	V_p/V_s
Sediment	0-2	0.5-1.5	0.5-1.5	2.00-3.00
Basement	0-3	1.8-2.8	1.8-2.8	1.65-2.00
Upper crust	3-20	3.0-3.8	3.0-3.9	1.65-1.80
Middle crust	4-20	3.4-4.3	3.4-4.4	1.65-1.80
Lower crust	5-15	3.5-4.8	3.6-4.9	1.65-1.80
Mantle	5-20	4.0-5.0	4.0-5.0	1.70-1.90

773 **Table 2:** Summary of H-κ stacking and NA inversion results for the current study.

Basic station information					Results				
Type	Station name	Lon (°)	Lat (°)	No of RFs	Moho Depth (km) (H-K stacking)	Bulk Vp/Vs (H-K stacking)	Moho Depth (km) (NA inversion)	Quality (NA inversion)	Moho type (NA inversion)
Temporary stations	BA02	145.20	-40.95	9	23.2±5.0	1.83±0.31	-	Moderate	Not evident
	BA03	145.84	-41.20	8	-	-	-	Moderate	Not evident
	BA07	148.31	-40.43	6	32.5±0.1	1.70±0.02	28	Good	Sharp
	BA08	147.97	-39.77	8	31.9±0.1	1.70±0.07	-	Poor	-
	BA09	147.32	-39.47	8	32.8±1.7	1.71±0.07	32	Good	Sharp
	BA11	143.98	-39.64	12	30.5±2.1	1.65±0.07	-	-	-
	BA13	148.83	-37.63	24	37.7±2.9	1.74±0.10	40	Good	Sharp
	BA17	146.33	-39.04	20	30.9±2.5	1.76±0.10	29	Good	Broad
	BA18	146.14	-38.02	3	-	-	38	Good	Sharp
	BA19	145.69	-38.57	20	25.5±2.4	1.93±0.14	-	Good	Not evident
	BA20	144.92	-38.42	30	26.3±1.6	1.93±0.12	29	Good	Sharp
	BA22	143.61	-37.99	5	-	-	29	Poor	Sharp
	BA24	142.54	-38.26	4	-	-	33	Poor	Sharp
Permanent stations	TAU	147.32	-42.91	41	33.5±1.9	1.70±0.08	33	Poor	Intermediate
	MOO	147.19	-42.44	58	33.0±1.2	1.71±0.04	34	Good	Sharp
	TOO	145.59	-37.57	276	37.5±1.2	1.68±0.04	36	Good	Sharp
	YNG	148.40	-34.20	178	37.3±0.5	1.76±0.04	35	Good	Sharp
	CAN	149.00	-35.32	402	39.1±0.5	1.73±0.02	40	Good	Sharp
	CNB	149.36	-35.32	155	38.5±1.1	1.70±0.04	39	Good	Broad
	MILA	149.16	-37.05	4	37.6±2.1	1.73±0.06	-	-	-



774 Figure 1: Regional map of southeastern Australia that shows key geological boundaries and the location of observed
775 or inferred tectonic units (modified from Bello et al., 2019a). Thick black lines delineate structural boundaries and
776 the thick brown dashed line traces out the boundary of Van Diemen's Land. HF = Heathcote Fault; GF = Governor Fault; BF
777 = Bootheragandra Fault; KF = Koonenberry Fault; THZ = Torrens Hinge Zone; MA = Macquarie Arc, NVP =
778 Newer Volcanics Province;; KI = King Island and FI = Flinders Island in Bass Strait; WTT = West Tasmania
779 Terrane; ETT = East Tasmania Terrane; AL = Arthur Lineament; TFS = Tamar Fracture System and RCB = Rocky
780 Cape Block. Outcrop boundaries are sourced from Rawlinson et al. 2016.

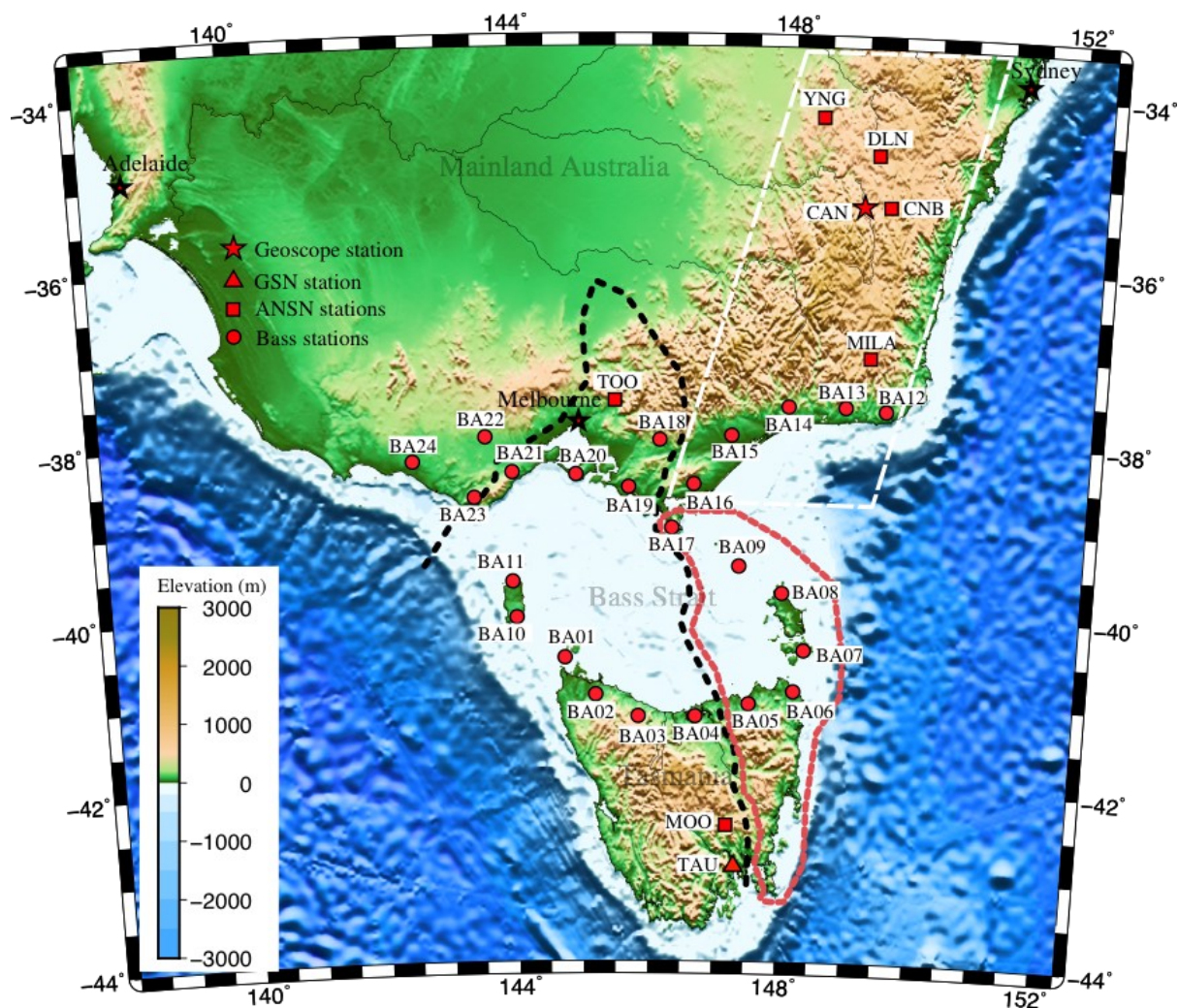
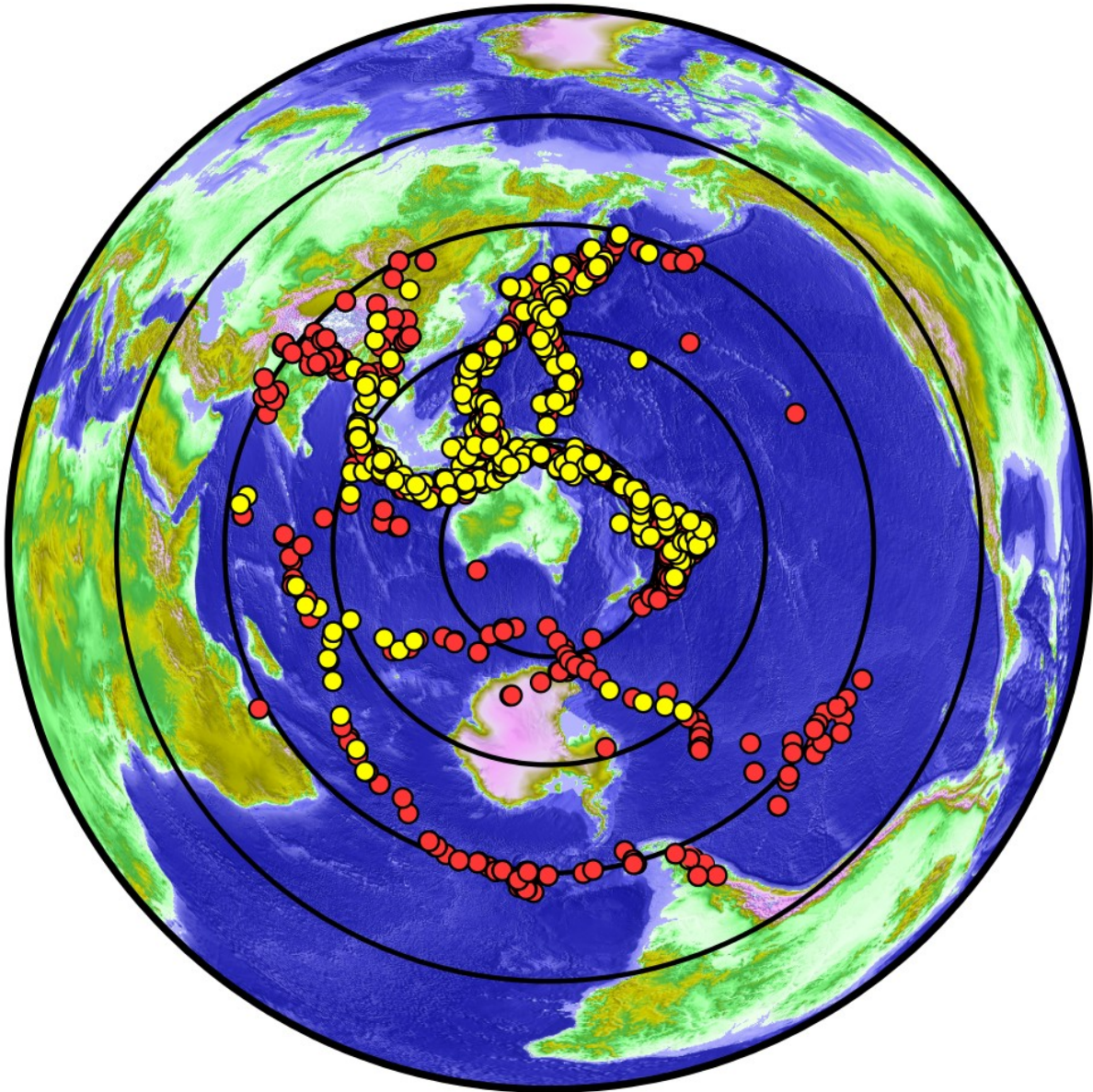
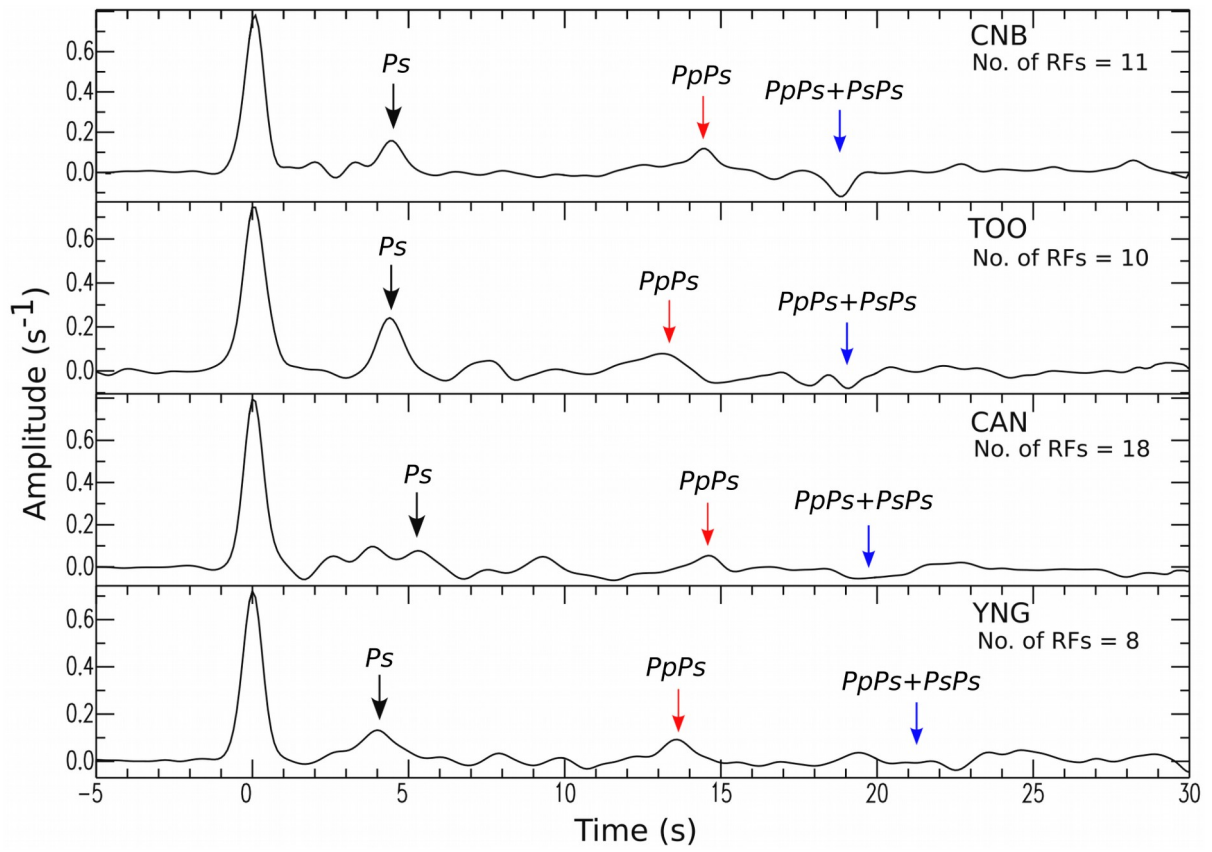


Figure 2: Location of seismic stations used in this study superimposed on a topographic/bathymetric map of southeast Australia (modified from Bello et al., 2019a). The boundary of VanDieland is delineated by a thick black dashed line. Thick red dashed line outlines the boundary of the East Tasmania Terrane and Furneaux Islands. Thick white dashed line highlights the eastern sector of the Lachlan Fold Belt. Topography/bathymetry is based on the ETOPO1 dataset (Amante and Eakins, 2009).



786 **Figure 3: Distribution of distant earthquakes (teleseisms) used in this study. The locations of events that are**
 787 **ultimately used for RF analysis are denoted by yellow dots. Concentric circles are plotted at 30° intervals from the**
 788 **centre of Bass Strait. Topography/bathymetry colours are based on the Etopo1 dataset (Amante and Eakins, 2009).**



789 **Figure 4: Stacked receiver functions from Australian National Seismic Network (ANSN) stations TOO, YNG, MOO**
790 **and GSN station TAU. Small arrows indicate arrival of the P_s (black), P_pP_s (red) and $P_pP_s + P_sP_s$ (blue) phases from**
791 **the Moho.**

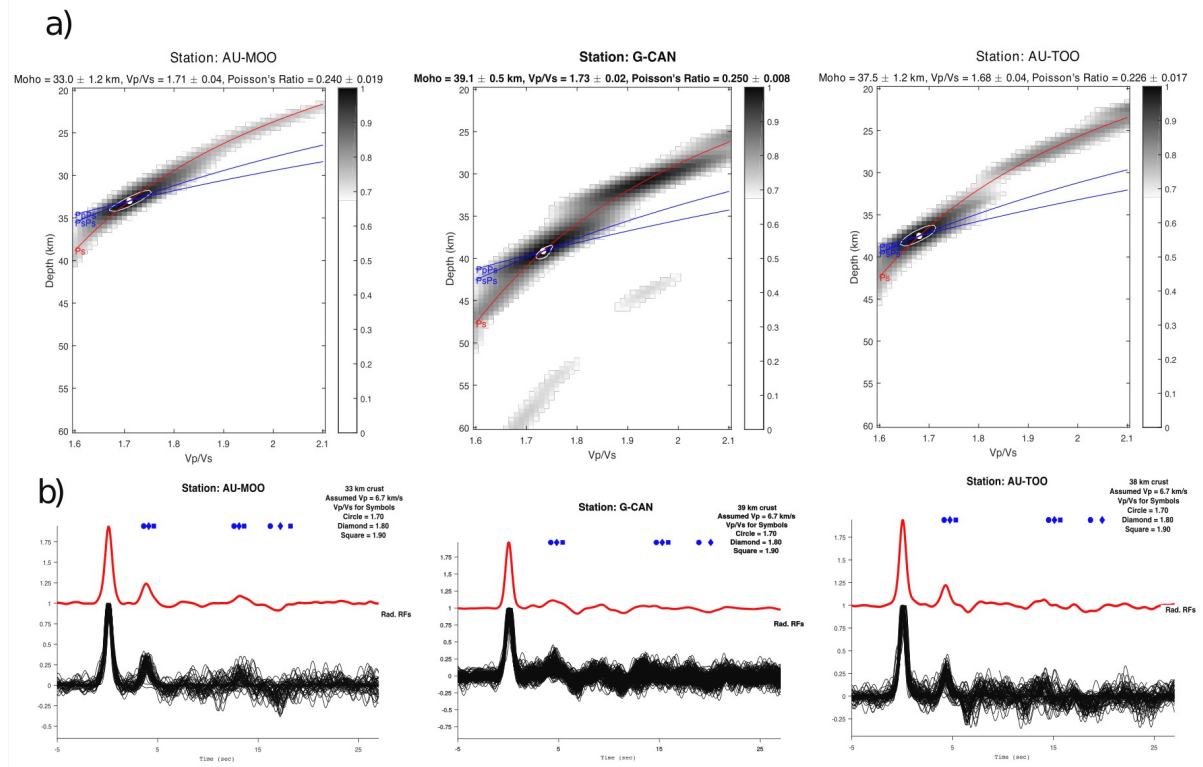
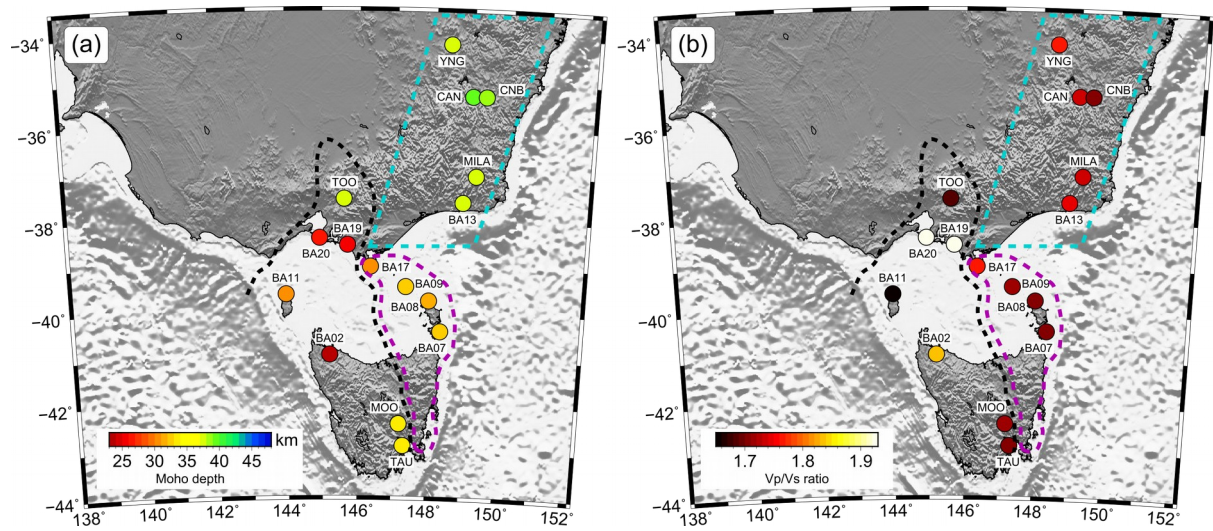
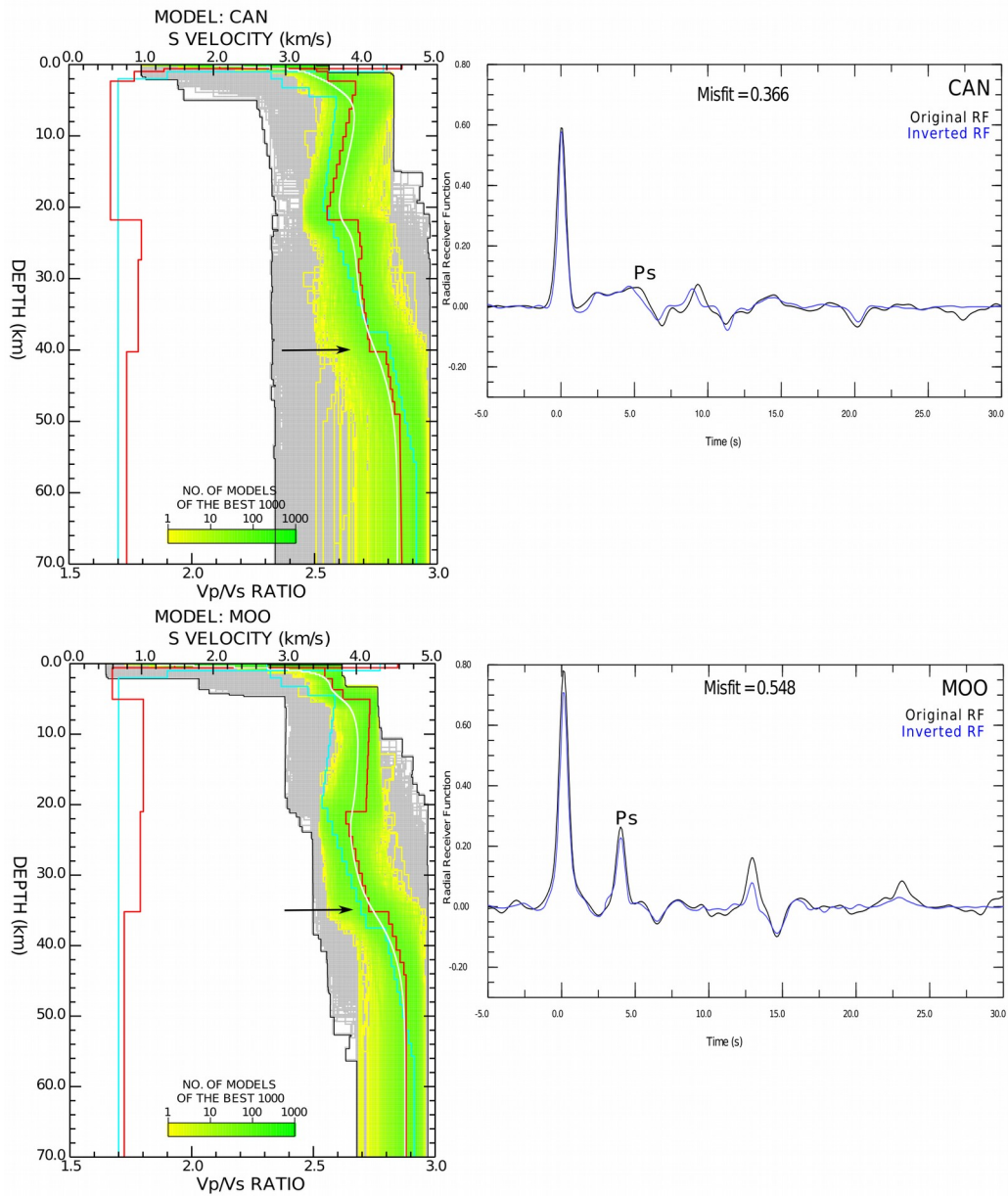


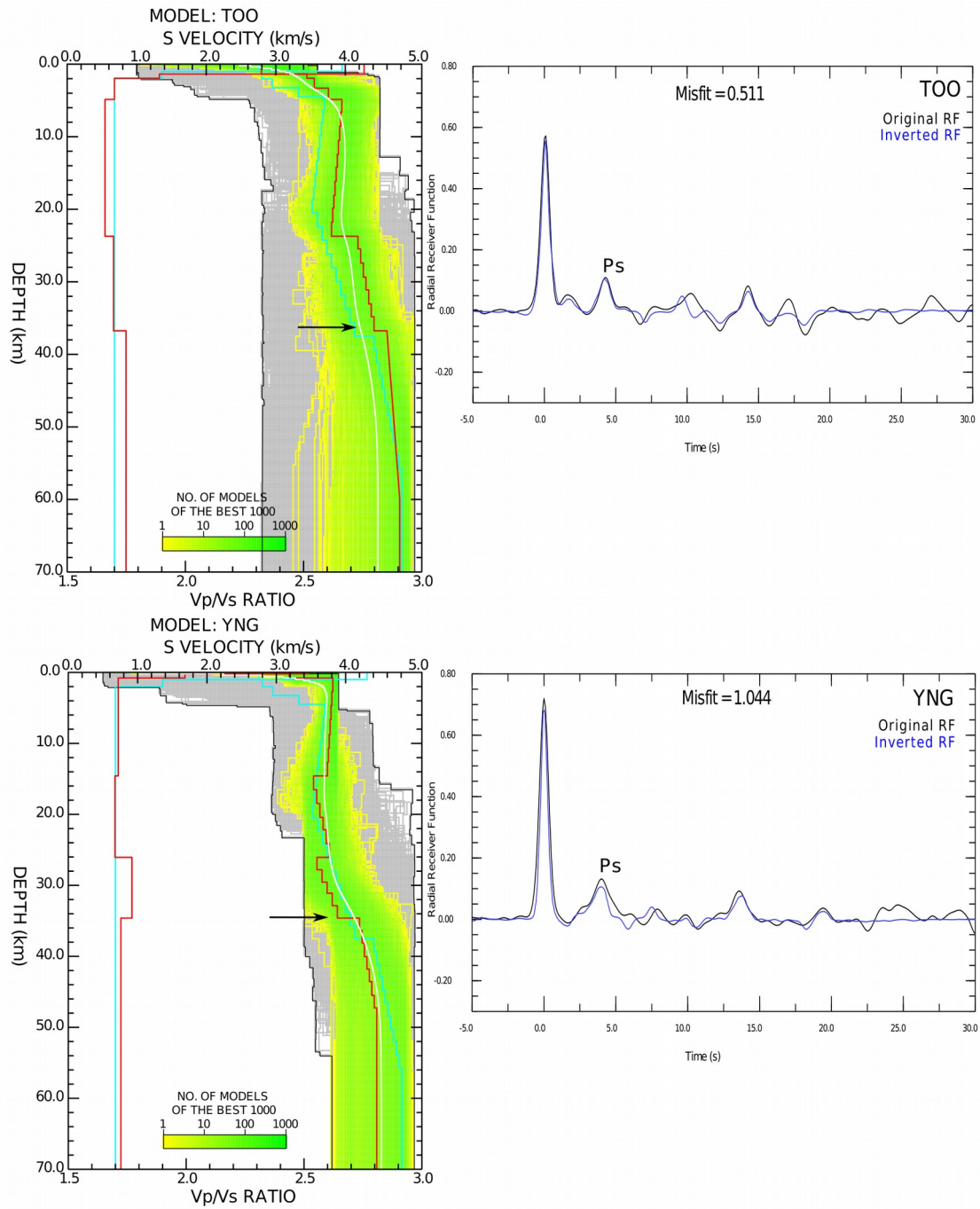
Figure 5: Results from the H - κ stacking analysis for RFs (Zhu and Kanamori, 2000) at stations MOO, CAN and TOO. In each case (a) normalised amplitudes of the stack over all back-azimuths along the travel time curves corresponding to the P_s and $PpPs$ phases. (b) Corresponding stacked receiver function for each station.



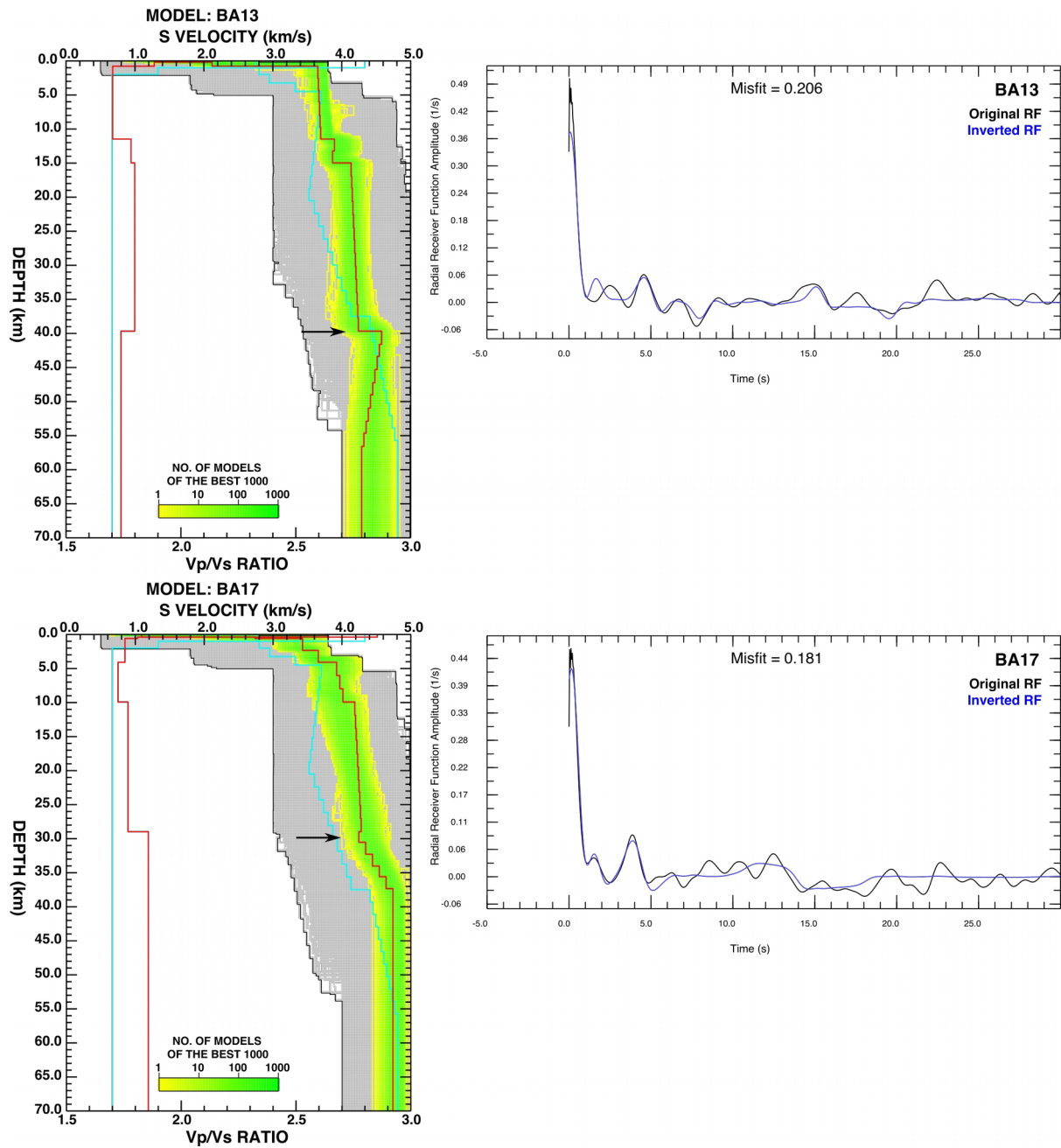
795 **Figure 6: (a) Variations in crustal thickness and (b) V_p/V_s ratio taken from the linear ($H-\kappa$) stacking results (Table 2).**
796 **Crustal thickness varies between ~23 and 39 km. V_p/V_s ratios vary from ~1.65 to 1.93. Thick black dashed line**
797 **denotes the boundary of VanDieland. Thick magenta dashed line outlines the boundary of East Tasmania Terrane**
798 **and eastern Bass Strait (ETT+EB). Thick cyan dashed line highlights the eastern part of the Lachlan Fold Belt.**
799 **Illuminated topography/bathymetry is based on the Etopo1 dataset (Amante and Eakins, 2009).**



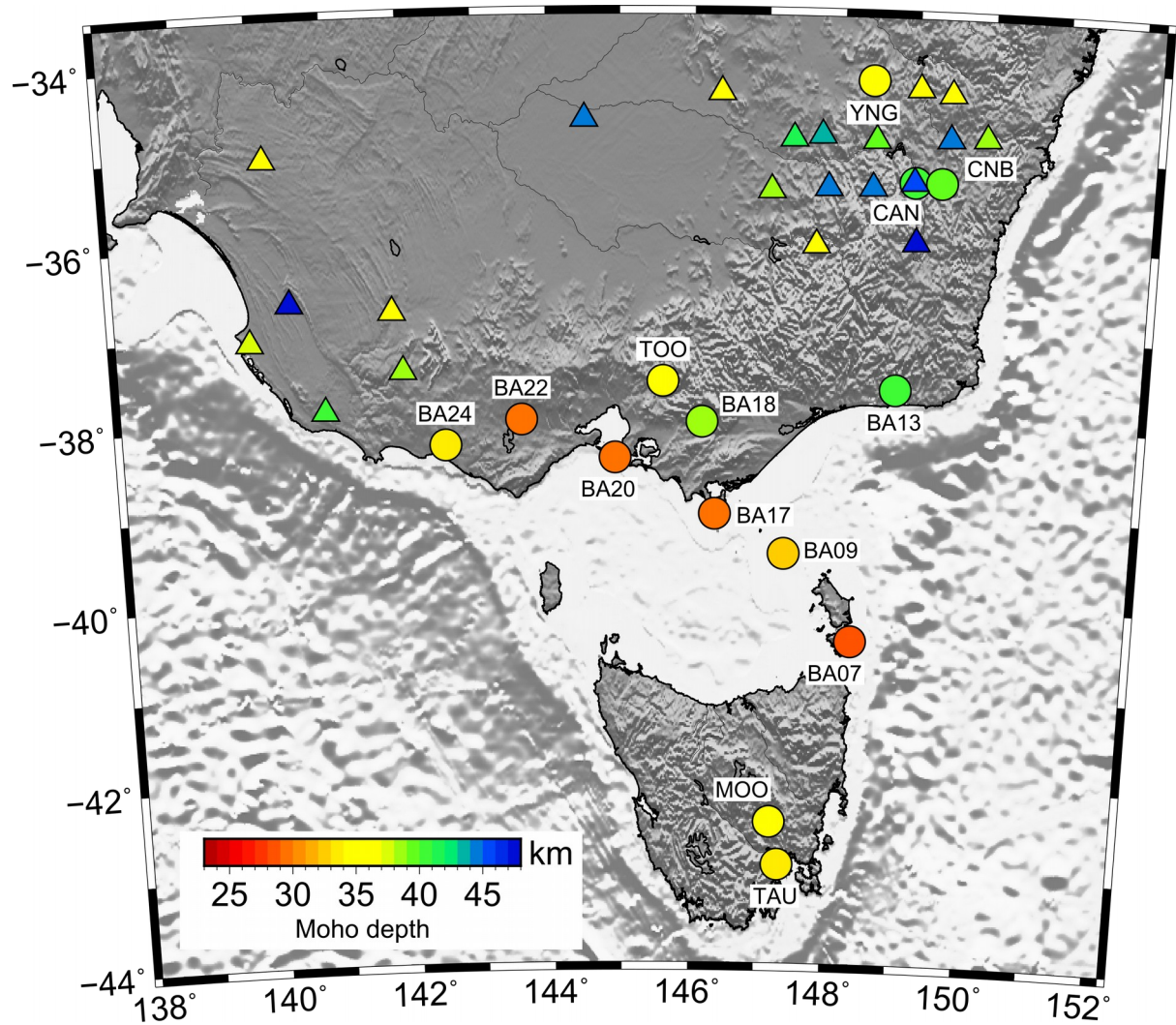
800 **Figure 7: (Left) Seismic velocity models for CAN and MOO stations obtained from the neighbourhood algorithm**
801 **(Sambridge 1999a). The grey area indicates all the models searched by the algorithm. The best 1000 models are**
802 **indicated by the yellow to green colours; the best one (smallest misfit) corresponds to the red line, both for S -wave**
803 **velocity (top horizontal axis) and V_p/V_s ratio (bottom horizontal axis) and the white line is the average velocity model.**
804 **(Right) Waveform matches between the observed stacked receiver functions (black) and predictions (blue) based on**
805 **the best models. “Misfit” refers to the chi-square estimate as defined by Equation 2.**



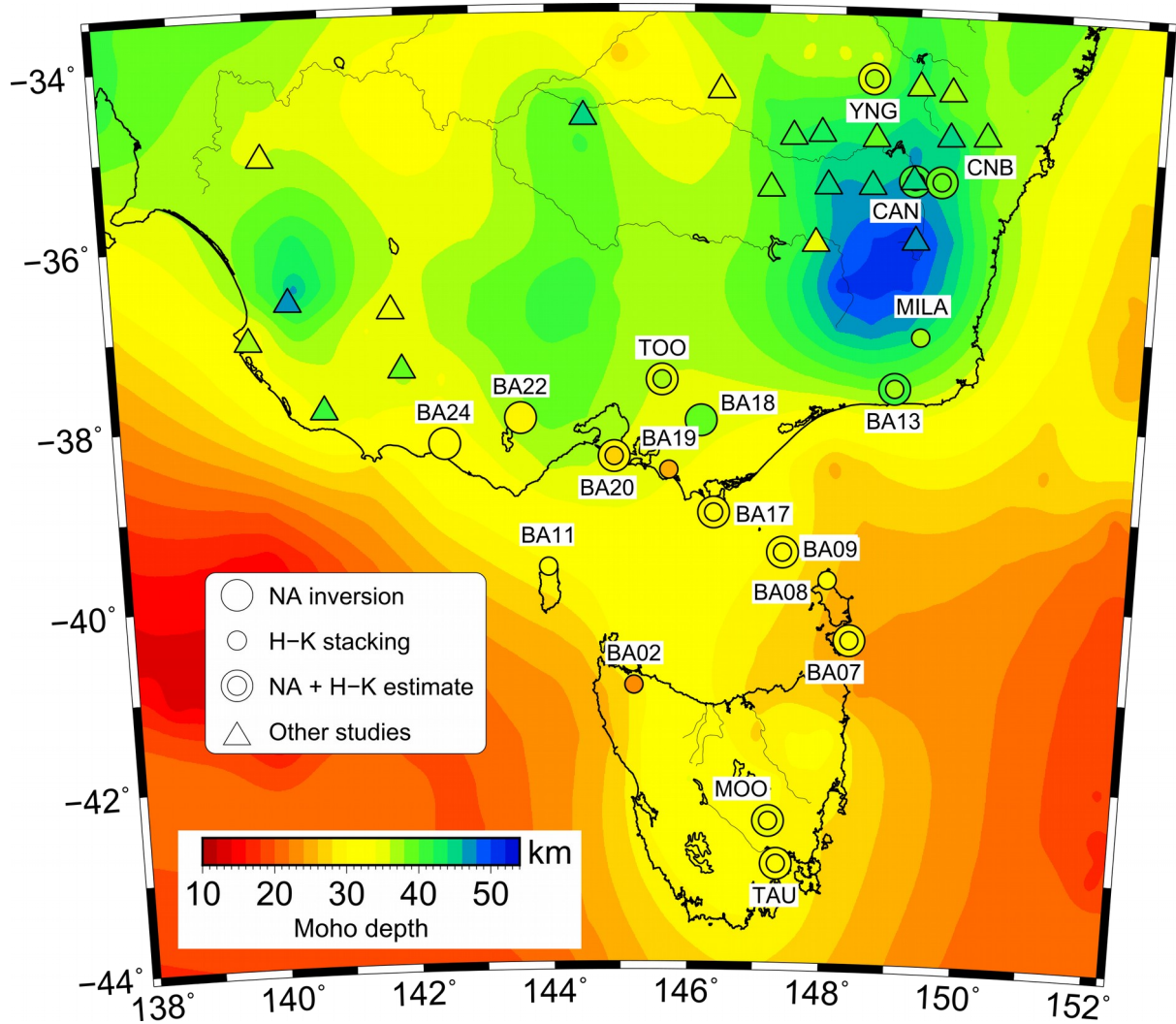
806 **Figure 8: (Left) Seismic velocity models for stations TOO and YNG obtained from the neighbourhood algorithm.**
807 **(Right) Comparison between the observed stacked and the predicted receiver functions from the NA inversion. See**
808 **Figure 7 caption for more details.**



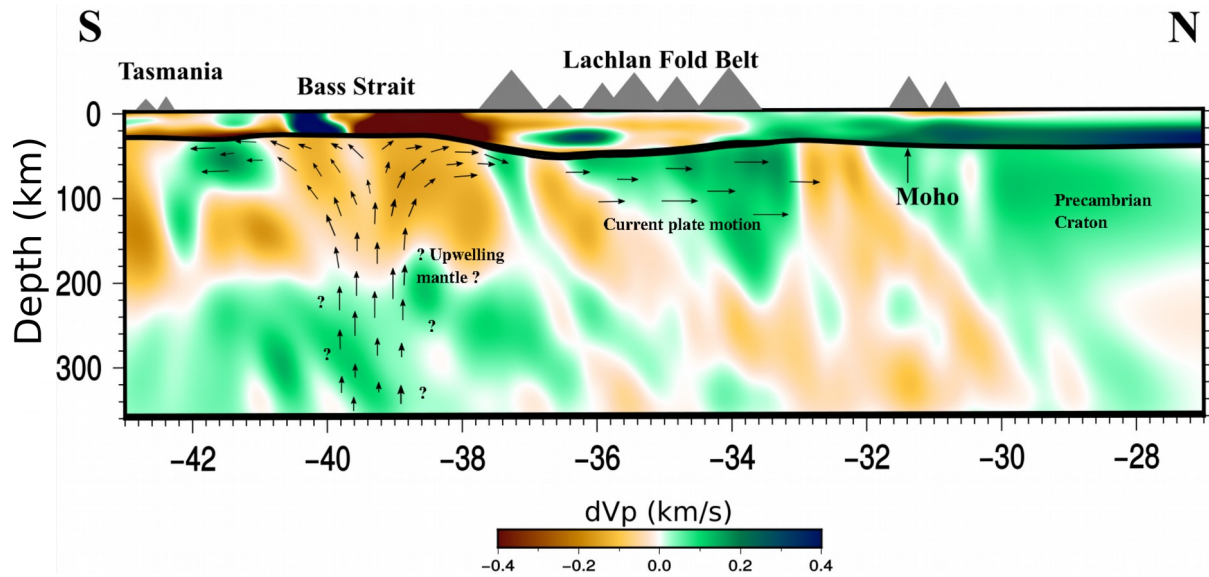
809 Figure 9: (Left) Seismic velocity models for temporary stations BA13 and BA17 obtained from the neighbourhood
810 algorithm. (Right) Comparison between the observed stacked and the predicted receiver functions from the NA
811 inversion. See Figure 7 caption for more details.



812 Figure 10: Map showing crustal thickness variations based on the S-wave velocity inversion results of this study
813 (stars) and previous studies (octagons) (Clitheroe et al., 2000, Fontaine et al., 2013a,b; Shibitani, 1996; Tkalcic et al,
814 2013). Topography/bathymetry is based on the Etopo1 dataset (Amante and Eakins, 2009).



815 Figure 11: Comparison between the AusMoho model (background colour map) and Moho depths determined
 816 through RF analysis in this and previous studies. Small coloured circles denote the Moho depths determined from
 817 H- κ stacking, whereas large coloured circles correspond to receiver function estimates. When both H- κ and NA-
 818 derived depths are available at a single station, the smaller H- κ circle is superimposed on the larger NA circle, so that
 819 both depths can be observed on the one plot. Moho depths determined from previous RF studies are denoted by
 820 triangles.



821 Figure 12: Composite result of teleseismic tomography (mantle velocity anomalies), ambient noise (crustal velocity
822 anomalies), receiver functions (Moho) and shear wave splitting (inferred mantle flow relative to over-riding plate).
823 Velocity slices are taken at 148°E.